Forschungszentrum Karlsruhe
Technik und Umwelt
Wissenschaftliche Berichte
FZKA 5832

A Boundary Collocation Study of the Edge-bonded Plate of Dissimilar Materials

T. Fett
Institut für Materialforschung

Oktober 1996

FORSCHUNGSZENTRUM KARLSRUHE
Technik und Umwelt
Wissenschaftliche Berichte
FZKA 5832

A Boundary Collocation study of the edge-bonded plate of dissimilar materials

T. Fett

Institut für Materialforschung

Forschungszentrum Karlsruhe GmbH, Karlsruhe
1996

Forschungszentrum Karlsruhe GmbH
Postfach 3640, 76021 Karlsruhe

ISSN 0947-8620

Abstract

In components made of two bonded dissimilar materials singular stresses occur near the free edges in case of thermal and mechanical loadings. In this report the stresses in a rectangular plate will be studied using the Boundary Collocation Method (BCM) for different types of externally applied tractions at the ends. The eigenvalues of the Airy stress function, necessary for an eigenfunction expansion of the stresses in the BCM, will be considered in detail. The stress intensity factors characterising the strongness of the stress singularity will be computed and the influence of the ratio of plate length to plate width will be analysed.

Eine Boundary Collocation Studie der rechteckigen Platte aus zwei verschiedenen Materialien

Zusammenfassung

In Bauteilen, die aus zwei verschiedenen Materialien hergestellt werden, können infolge thermischer und mechanischer Belastungen singuläre Spannungen nahe der freien Oberfläche auftreten. Im vorliegenden Bericht wird der für die Praxis besonders wichtige Fall der rechteckigen Platte betrachtet. Der Spannungszustand wird für unterschiedliche mechanische Belastungen an den Plattenenden mithilfe der Boundary Collocation Methode (BCM) untersucht. Die für die BCM notwendigen Eigenwerte der Airy'schen Spannungsfunktion werden berechnet und der die Stärke der Singularität charakterisierende Spannungsintensitätsfaktor ermittelt. Als spezielle geometrische Einflußgröße wird der Einfluß des Verhältnisses von Plattenhöhe zu Plattenbreite studiert.

Contents

1. Introduction

In components made of two bonded dissimilar materials singular stresses occur near the free edges in case of thermal and mechanical loadings.
The stress state very close to the free edge can be computed analytically as had been shown very early by several authors [1]-[3]. Their analyses allow the shape of the stress distribution to be determined with respect to the distance r from the edge and the angle φ (see fig.1) to the interface.
Mizuno et al. [4] introduced a stress intensity factor K which represents the intensity of the singular stress part.
In all analytical considerations one quantity, the stress intensity factor K, remained undetermined. For its computation different numerical procedures were applied.
Yang [5] and Munz and Yang [6] used the FE-method and evaluated - besides the rectangular plate - a large number of components with different angles between the two free surfaces and the interface line. Rectangular plates with different height to width ratios were analysed by Tilscher et al. [7] and Heinzelmann et al. [8].
Blanchard and Ghoniem [9][10] applied a Boundary Collocation procedure for symmetrical loadings modelling one half of a rectangular plate.
A method was described in [11] which is based on the condition that the loadings near the opposite free edge, caused by the singular stress term, should be balanced by regular stress terms. Only very slow convergence could be reached.
A weight function procedure was developed by Banks-Sills et al. [12] which relies on the dislocation method proposed by Hein and Erdogan [3].
In the special case of thermal loading where the stresses occur by mismatch in the thermal expansion coefficients a series expansion of the total stress field includes a constant stress term which can be determined analytically (see [4],[13]). Regular stress terms for complicated structures were presented by Munz et al. [14].
In this report the stresses in a rectangular plate will be studied using the Boundary Collocation Method (BCM) for different types of externally applied tractions at the ends. The eigenvalues, necessary for an eigenfunction expansion of the stresses in the BCM, will be considered in detail. The influence of plate length H to plate width $2L$ (see fig.1) will be of special interest.

2. Stress function and stresses

2.1 General relations

In this report the stresses in a rectangular bi-material plate (fig.1) are investigated for the case of tensile tractions at the lower and upper bounds. Different stress distributions will be considered.

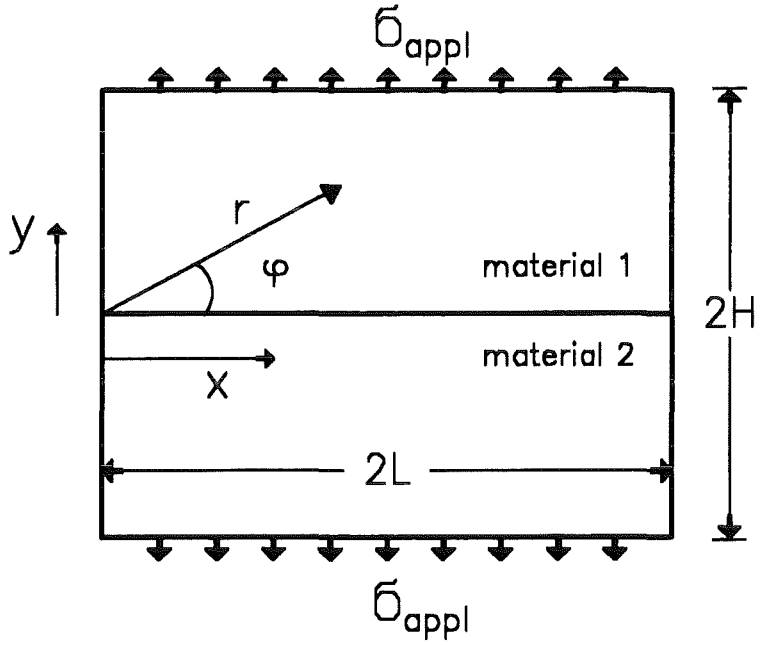

Figure 1. Geometry. Rectangular plate made from dissimilar materials.

The stress state in an edge-bonded plate made of two dissimilar materials is known if the Airy stress function Φ is known. The stress function can be obtained by solving the equation of compatibility

$$\Delta\Delta\Phi = 0 \tag{1}$$

in each of the materials separately. From a list of eigensolutions of the bipotential equation (see e.g. [15]) we use for a series expansion

$$\Phi = L^2 \sum_{k=0}^{\infty} (r/L)^{\lambda_k+1}[A_k \sin((1-\lambda_k)\varphi) + B_k \cos((1-\lambda_k)\varphi) + C_k \sin((1+\lambda_k)\varphi) + D_k \cos((1+\lambda_k)\varphi)] \tag{2}$$

where the coefficients A_k ... D_k and the eigenvalues λ_k are complex, i.e.

$$\begin{aligned} A_k &= A_k^R + iA_k^I \\ B_k &= B_k^R + iB_k^I \\ C_k &= C_k^R + iC_k^I \\ D_k &= D_k^R + iD_k^I \end{aligned} \tag{3}$$

and

$$\lambda_k = t_k + ip_k \tag{4}$$

The stresses result from

$$\sigma_r = \frac{1}{r}\frac{\partial \Phi}{\partial r} + \frac{1}{r^2}\frac{\partial^2 \Phi}{\partial \varphi^2} \tag{5}$$

$$\sigma_\varphi = \frac{\partial^2 \Phi}{\partial r^2} \tag{6}$$

$$\tau_{r\varphi} = \frac{1}{r^2}\frac{\partial \Phi}{\partial \varphi} - \frac{1}{r}\frac{\partial^2 \Phi}{\partial r \partial \varphi} \tag{7}$$

From the stresses also the displacements u and v can be determined. They are obtained from the relation between strains and displacements

$$\begin{aligned} \varepsilon_r &= \frac{\partial u}{\partial r} \\ \varepsilon_\varphi &= \frac{u}{r} + \frac{\partial v}{r\,\partial \varphi} \\ \gamma &= \frac{\partial v}{\partial r} - \frac{v}{r} + \frac{1}{r}\frac{\partial u}{\partial \varphi} \end{aligned} \tag{8}$$

and application of Hooke's law. The stresses and displacements have to satisfy the following boundary conditions

$$\sigma_{1\varphi}(r, \varphi = \pi/2) = 0 \quad , \quad \tau_{1,\, r\varphi}(r, \pi/2) = 0$$

$$\sigma_{2\varphi}(r, \varphi = -\pi/2) = 0 \quad , \quad \tau_{2,\, r\varphi}(r, -\pi/2) = 0$$

$$\sigma_{1\varphi}(r, \varphi = 0) = \sigma_{2\varphi}(r,0) \quad , \quad \tau_{1,\, r\varphi}(r, 0) = \tau_{2,\, r\varphi}(r,0) \tag{9}$$

$$u_1(r, \varphi = 0) = u_2(r,0) \quad , \quad v_1(r, 0) = v_2(r,0)$$

where the subscripts 1 and 2 refer to materials 1 and 2. These eight boundary conditions lead to a homogeneous system of linear equations of rank 7

$$\underline{X}\mathbf{A}_k = 0 \quad , \quad \mathbf{A}_k = (A_{1k}, B_{1k}, C_{1k}, D_{1k}, A_{2k}, B_{2k}, C_{2k}, D_{2k})^T \tag{10}$$

from which the eigenvalue λ_k and seven of the eight coefficients can be determined. Since the rank is 7, one coefficent can be freely chosen. Let us set $A_{1k} = 1$ (i.e. $A^R_{1k} = 1$, $A^I_{1k} = 0$). From the disappearing determinant

$$\det(\underline{X}) = 0 \tag{11}$$

one obtains [4]

$$F(\lambda_k) = \lambda_k^2(\lambda_k^2 - 1)\alpha^2 + 2\lambda_k^2[\sin^2(\pi\lambda_k/2) - \lambda_k^2]\alpha\beta$$

$$+ [\sin^2(\pi\lambda_k/2) - \lambda_k^2]^2\beta^2 + \sin^2(\pi\lambda_k/2)\cos^2(\pi\lambda_k/2) = 0 \tag{12}$$

The parameters α and β are the Dundurs parameters defined by

$$\alpha = \frac{m_2 - km_1}{m_2 + km_1} \tag{13}$$

$$\beta = \frac{(m_2 - 2) - k(m_1 - 2)}{m_2 + km_1} \tag{14}$$

with $k = G_2/G_1$ and

$$m_i = \begin{cases} \dfrac{4}{1 + \nu_i} & \text{for plane stress} \\ 4(1 - \nu_i) & \text{for plane strain} \end{cases} \tag{15}$$

G is the shear modulus and ν is the Poisson ratio. The trivial solution of eq.(12) is $\lambda = 0$. This eigenvalue is responsible for the constant stress term occurring under thermal loading. In order to simplify the numbering of the eigenvalues we will omit this special solution in the following considerations.
Since the relation $F(\lambda_k)$ is an <u>even</u> function of λ_k one obtains for any k two solutions, namely λ_k and $-\lambda_k$. In this investigation we restrict the solutions to those with positive real parts.

2.2 Determination of eigenvalues

The solutions of eq.(12) may be real and complex. Therefore, we use the general expression

$$\lambda_k = t_k + ip_k \tag{16}$$

with the real part t and the imaginar part p.

2.2.1 Real eigenvalues

Equation (12) provides a relation between α and β for an arbitrarily prescribed real eigenvalue $\lambda_k = t_k$, i.e. $p_k = 0$. With the abbreviations

$$\begin{aligned} A &= \lambda_k^2(\lambda_k^2 - 1) \\ B &= \lambda_k^2[\,\sin^2(\pi\lambda_k/2) - \lambda_k^2] \\ C &= [\,\sin^2(\pi\lambda_k/2) - \lambda_k^2]^2 \\ D &= \sin^2(\pi\lambda_k/2)\cos^2(\pi\lambda_k/2) \end{aligned} \tag{17}$$

one obtains

$$\beta_{1/2} = -B/C\,\alpha \pm \sqrt{(B^2/C^2 - A/C)\alpha^2 - D/C} \tag{18}$$

2.2.1.1 Real integer eigenvalues

In case of odd integer t_k one finds

$$\beta_1 = \frac{t_k}{t_k - 1}\alpha\,, \qquad \beta_2 = \frac{t_k}{t_k + 1}\alpha \tag{19}$$

For $t = 1$ ($\omega = 0$) the straight lines

$$\alpha = 0\,, \quad \text{and} \quad \beta = \alpha/2 \tag{20}$$

result. In case of even integer t_k we find

$$\beta_1 = \frac{t_k + 1}{t_k}\alpha\,, \qquad \beta_2 = \frac{t_k - 1}{t_k}\alpha \tag{21}$$

Since for even and odd eigenvalues the limit $t_k \to \infty$ yields $\beta_1 = \beta_2 = \alpha$, the higher order eigenvalues concentrate more and more near the line $\beta = \alpha$.

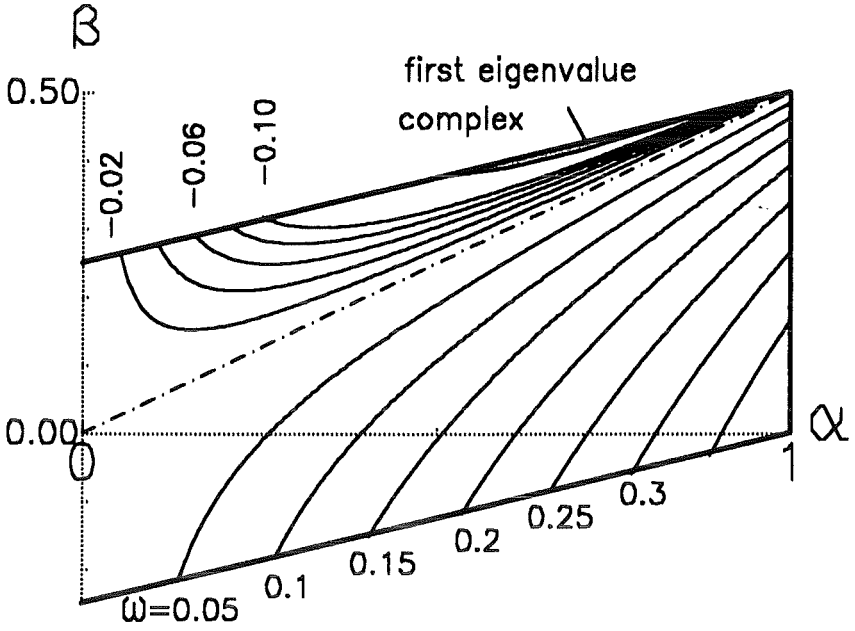

Figure 2. Eigenvalues. First eigenvalue, represented by ω, eq.(22) (third and fourth quadrants mirror-inverted).

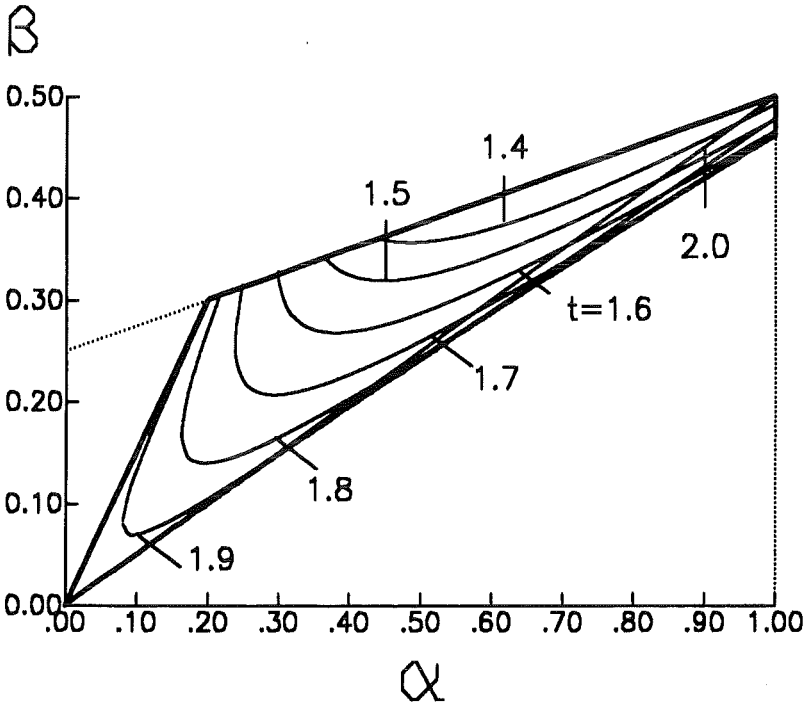

Figure 3. Eigenvalues. Range of Dundur's parameters for real eigenvalues $t \leq 2$ (only first quadrant plotted).

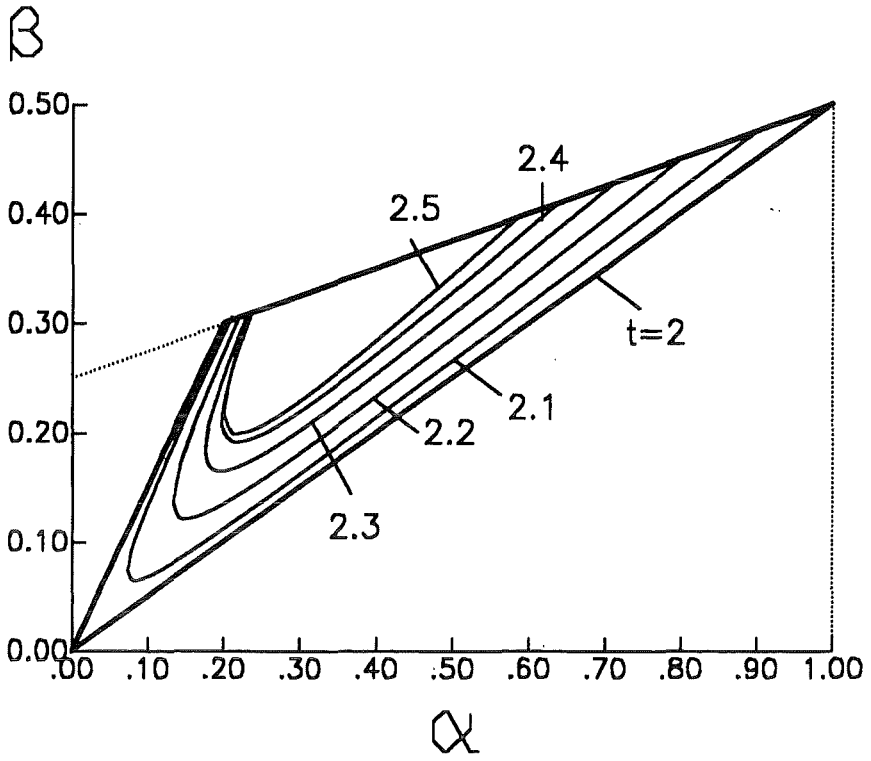

Figure 4. Eigenvalues. Range of Dundur's parameters for real eigenvalues $2 \leq t < 2.5$.

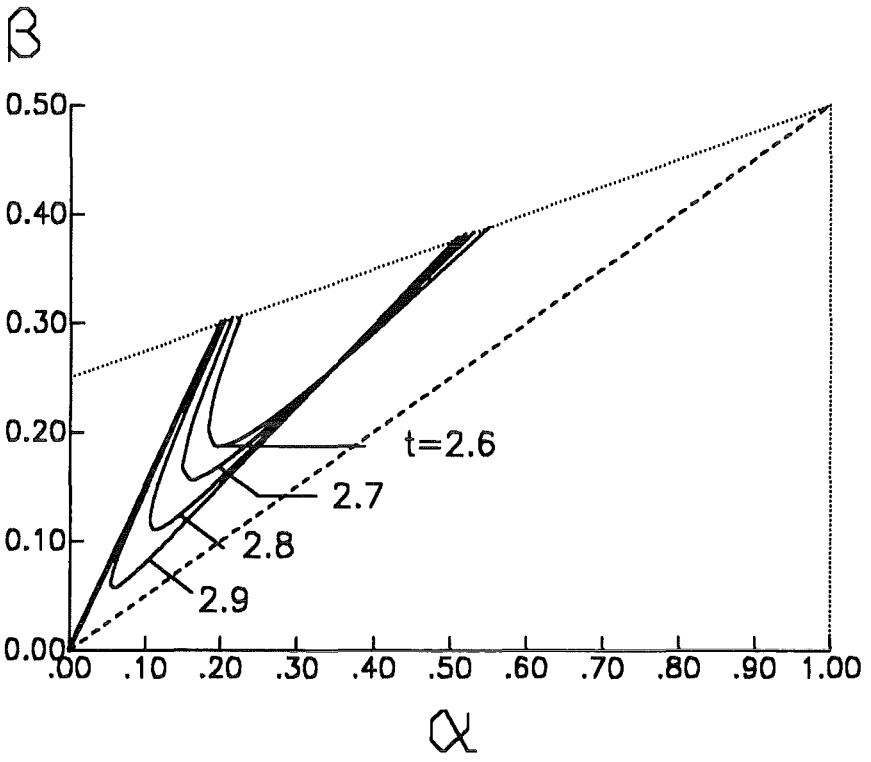

Figure 5. Eigenvalues. Range of Dundur's parameters for real eigenvalues $2.5 \leq t < 3$.

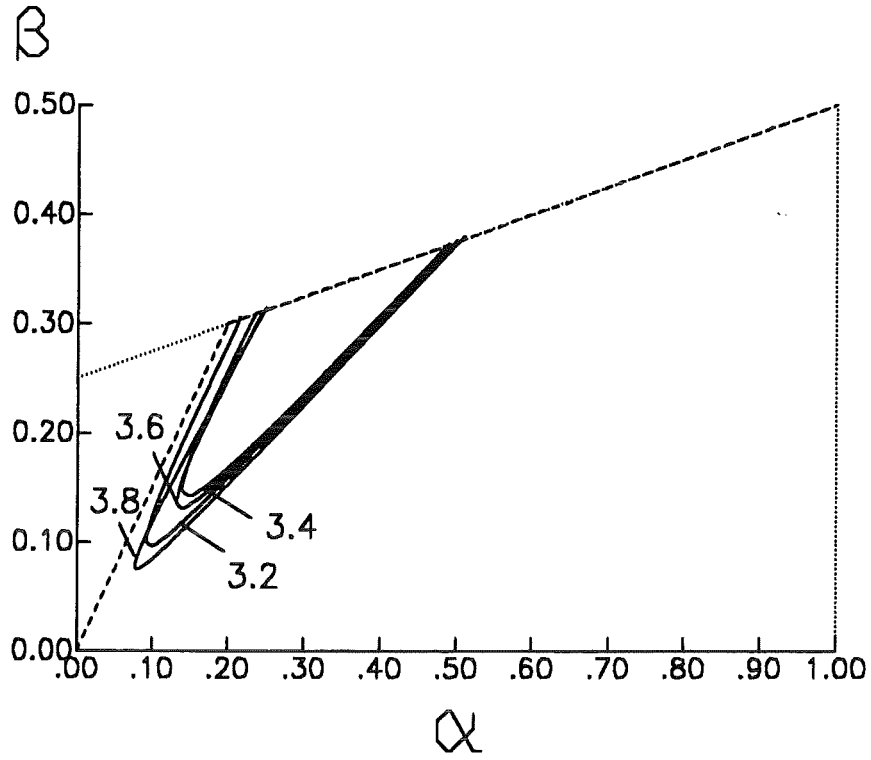

Figure 6. Eigenvalues. Range of Dundur's parameters for real eigenvalues $3 < t < 4$.

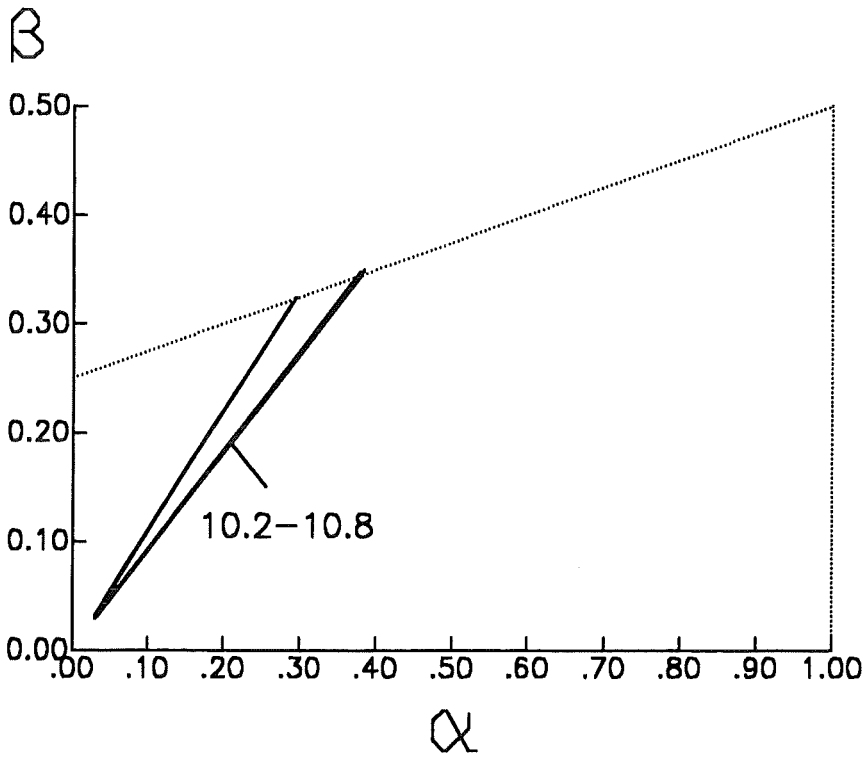

Figure 7. Eigenvalues. Range of Dundur's parameters for large real eigenvalues $10 < t < 11$.

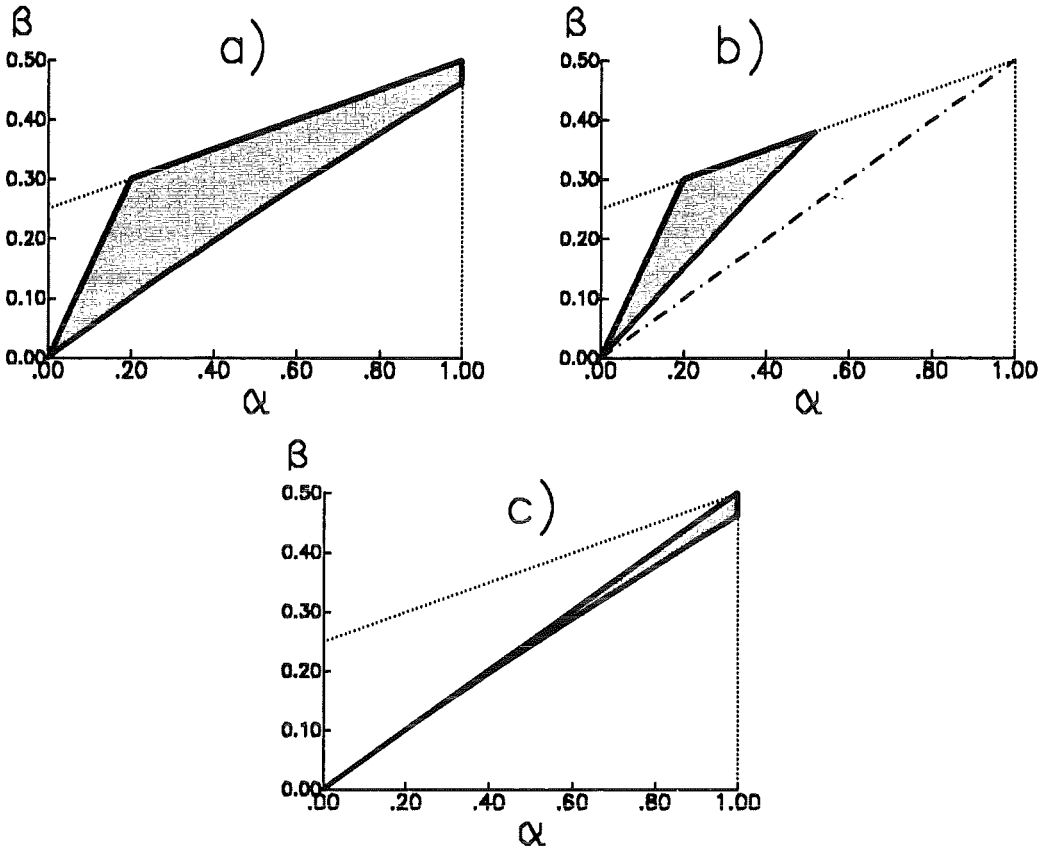

Figure 8. Eigenvalues. Range of Dundur's parameters in which real eigenvalues occur: a) second and third eigenvalues; b) fourth eigenvalue; c) real eigenvalues and positive ω.

2.2.1.2 Real non-integer eigenvalues

The first eigenvalue is a real one ($p = 0$) for all material combinations. It defines the stress exponent ω by

$$\omega = 1 - \mathrm{Re}(\lambda) = 1 - t \tag{22}$$

This eigenvalue leads to the singular stress term with $t < 1$ and $\omega > 0$ if $\beta < \alpha/2$ (see fig.2). For $\beta > \alpha/2$ the singular behaviour disappears since the first eigenvalue is positive $t > 1$ ($\Rightarrow \omega > 0$) (see e.g. [6]). There remains a small area in the α-β-diagram (shaded area in fig.2) where no real first eigenvalues occur [16]. In fig.2 the first and second quadrants are shown. The third and the fourth quadrants contain identical curves with the symmetry condition $\omega(-\alpha, -\beta) = \omega(\alpha, \beta)$. For special material combinations the next following eigenvalues may also be real. The range of combinations of Dundurs parameters in which (besides the conjugate complex eigenvalues) also real eigenvalues occur is shown in fig.3. In this and in the following diagrams only the first quadrant is plotted. The same data occur in the third quadrant which is mirror-inverted to the first (i.e. $t(-\alpha, -\beta) = t(\alpha, \beta)$). The area in the $\alpha - \beta$ –diagram is bounded by the lines:

$$\beta = 3/2\alpha$$

$$\beta = 1/4\alpha + 1/4 \qquad (23)$$

$$\beta \simeq \alpha/2 - 0.0384\alpha^{2.2}$$

The whole area belongs to the second eigenvalue, the third real eigenvalue covers nearly the same area (but $\beta > \alpha/2$). In fig.3 curves for constant values t (second eigenvalue) are entered and figs.4 and 5 represent the third real eigenvalue. Higher-order eigenvalues fill only parts of this area (see figs.6 and 7). The fact that the higher real eigenvalues are concentrated near the line $\beta = \alpha$ can also be seen from fig.7 which represents eigenvalues in the range $11 < t < 12$. Figure 8 shows the area in the $\alpha - \beta -$ diagram in which the second and third real eigenvalues, part a), and the fourth and higher real eigenvalues, part b), occur. The upper boundaries of the area are identical with those of fig.3. The lower line, part b), is approximately given by $\beta \simeq 3/4\alpha$. A more accurate description is

$$\beta = 3/2\alpha$$

$$\beta = 1/4\alpha + 1/4 \qquad (24)$$

$$\beta \simeq 3/4\alpha - 0.0195\alpha^{2.5}$$

Finally, fig.3c shows the region where for positive singularity exponents ω additional real eigenvalues can be found, i.e. the region expressed by

$$\alpha/2 - 0.038\alpha^{2.2} < \beta < \alpha/2 \qquad (25)$$

It should be noted that for any point in this range <u>two</u> solutions are obtained since the lines in fig.3 intersect. As an example, we have for the combination ($\alpha = 0.998$, $\beta = 0.474$) the two eigenvalues $t = 1.521$ and $t = 1.878$. This has to be taken into consideration in a numerical analysis.

2.2.2 Complex eigenvalues

This allows the complex function F to be written

$$F(t_k, p_k) = \mathrm{Re}(F) + i\,\mathrm{Im}(F) = 0 \qquad (26)$$

In order to allow a separation to be made into real and imaginary parts, we have to use the relations

$$\begin{aligned} \sin(t \pm ip) &= \sin(t)\ \cosh(p) \pm i\ \cos(t)\ \sinh(p) \\ \cos(t \pm ip) &= \cos(t)\ \cosh(p) \mp i\ \sin(t)\ \sinh(p) \end{aligned} \qquad (27)$$

For the evaluation of eq.(26) two zero-routines were used, one being stacked into the other. While the outer zero-routine provided a starting value for t, the inner routine determined the related value of p which made up the part $\mathrm{Im}(F) = 0$. In the outer routine

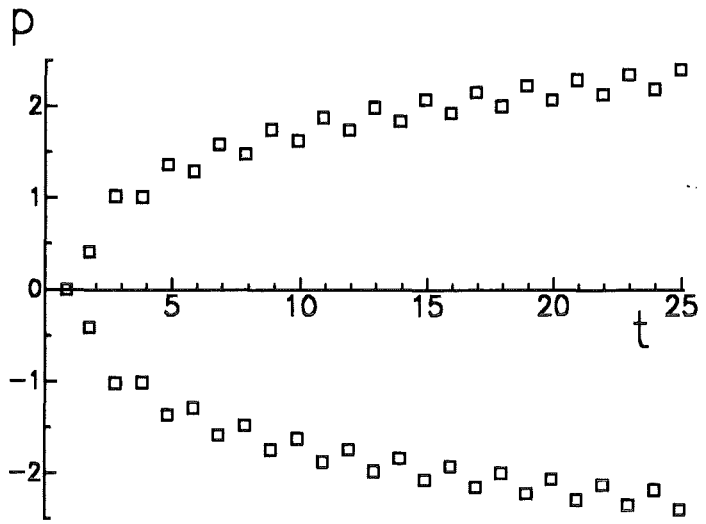

Figure 9. Eigenvalues. Real and imaginary parts of the eigenvalues λ computed with $E_2/E_1 = 10$, $\nu_1 = \nu_2 = 0.3$ eigenvalues with negative real part $t < 0$ ignored.

the value of t was changed until the real part disappeared, too. The results are represented in fig.9 for a realistic material combination. The determination of the eigenvalues λ_k will be demonstrated for the case

$$E_2/E_1 = 10\,,\ \nu_1 = \nu_2 = 0.3 \tag{28}$$

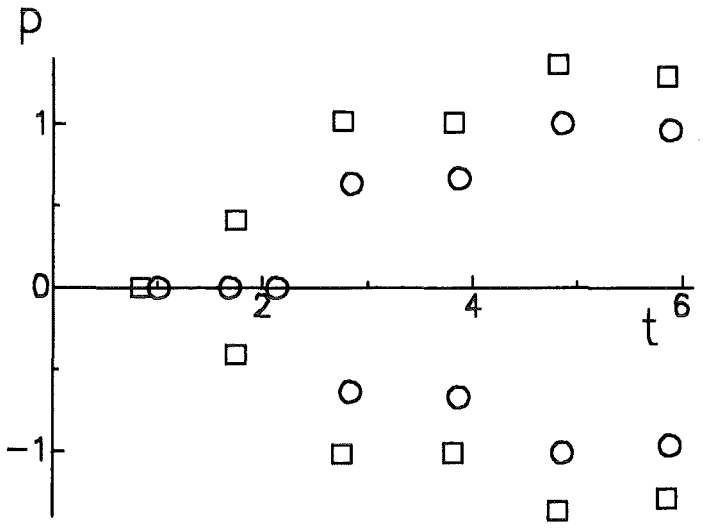

Figure 10. Eigenvalues. Real and imaginary parts of the eigenvalues λ computed with data-set B, eq.(29) (circles), compared with the results of fig.9 (squares).

These data are subsequently named "data-set A". We find for the real eigenvalue $t = 0.8408 (\Rightarrow \omega = 0.1592)$. The following eigenvalues appear as complex conjugates, as reported by Blanchard and Ghoniem [10]. An additional material combination was taken from the area described by eq.(23). The parameters were chosen as:

$$E_2/E_1 = 2.5\,,\ \nu_1 = 0.1\,,\ \nu_2 = 0.4 \tag{29}$$

named "data-set B". The Dundurs parameters resulting for plane stress are $\alpha = 0.4286$ and $\beta = 0.2357$. For the real terms we find $t = 1.0176$ $(\omega = -0.0176)$, $t = 1.700$ and $t = 2.1373$. The first eigenvalues are plotted in fig.10 together with the first eigenvalues of fig.9.

2.3 Stress components and angular functions

2.3.1 General case

The coefficients defined by eq.(10) have to be determined by solving the system of linear equations. If these coefficients are known the stresses can be computed as

$$\sigma_{r,k} = (r/L)^{\lambda_k - 1}\,\lambda_k\,[A(3-\lambda_k)\sin((1-\lambda_k)\varphi) + B(3-\lambda_k)\cos((1-\lambda_k)\varphi) - C(1+\lambda_k)\sin((1+\lambda_k)\varphi) - D(1+\lambda_k)\cos((1+\lambda_k)\varphi)] \tag{30}$$

$$\sigma_{\varphi,k} = (r/L)^{\lambda_k - 1}\,\lambda_k(\lambda_k+1)\,[A\sin((1-\lambda_k)\varphi) + B\cos((1-\lambda_k)\varphi) + C\sin((1+\lambda_k)\varphi) + D\cos((1+\lambda_k)\varphi)] \tag{31}$$

$$\tau_k = -(r/L)^{\lambda_k - 1}\,\lambda_k\,[A(1-\lambda_k)\sin((1-\lambda_k)\varphi) - B(1-\lambda_k)\cos((1-\lambda_k)\varphi) + C(1+\lambda_k)\sin((1+\lambda_k)\varphi) - D(1+\lambda_k)\cos((1+\lambda_k)\varphi)] \tag{32}$$

2.3.2 Singular term

For the singular term $\lambda < 1$ the solution is real. Therefore, one can write

$$\sigma_{ij} = \frac{K}{(r/L)^{\omega}}\,\hat{\sigma}_{ij}(\varphi) \quad (+\sigma_{ij0}) \tag{33}$$

with the stress intensity factor K and the angular functions

$$\hat{\sigma}_r = \frac{A(2+\omega)\sin(\omega\varphi) + B(2+\omega)\cos(\omega\varphi) - C(2-\omega)\sin((2-\omega)\varphi) - D(2-\omega)\cos((2-\omega)\varphi)}{(2-\omega)(B+D)} \tag{34}$$

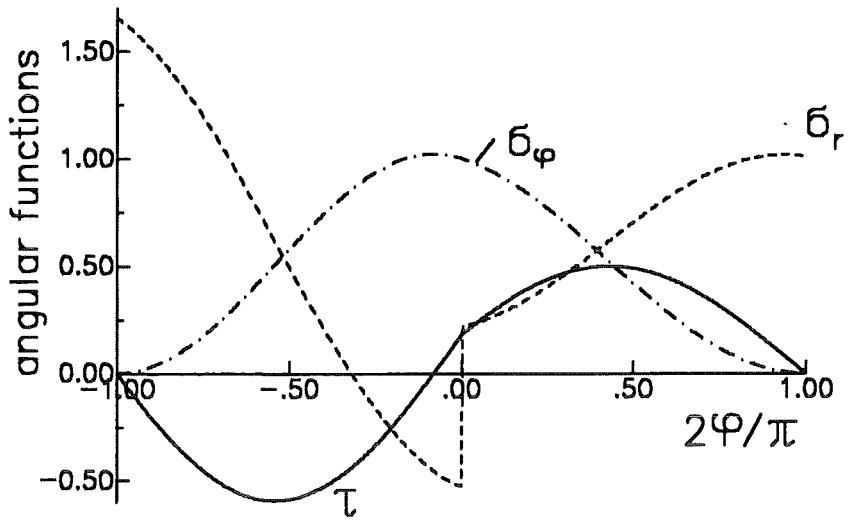

Figure 11. Angular functions. Angular functions for the singular stress terms, computed with $E_2/E_1 = 10$, $\nu_1 = \nu_2 = 0.3$.

$$\hat{\sigma}_\varphi = \frac{A\sin(\omega\varphi) + B\cos(\omega\varphi) + C\sin((2-\omega)\varphi) + D\cos((2-\omega)\varphi)}{B+D} \tag{35}$$

$$\hat{\tau} = -\frac{A\omega\cos(\omega\varphi) - B\omega\sin(\omega\varphi) + C(2-\omega)\cos((2-\omega)\varphi) - D(2-\omega)\sin((2-\omega)\varphi)}{(2-\omega)(B+D)} \tag{36}$$

Due to this definition the angular function for the circumferential stresses is $\hat{\sigma}_\varphi = 1$ for $\varphi = 0$. The constant stress term is present in case of thermal loading and has been calculated in [4]-[6]. The angular functions are plotted in fig.11.

2.3.3 Higher order terms

The higher order terms ($\lambda > 1$) are complex. To determine the stresses we have to introduce into eqs.(30)-(32):

- the complex eigenvalues as given by eq.(16),
- the relations eq.(27) for the complex sine and cosine terms,
- the complex coefficients according to eq.(3),
- and, finally, the substitution

$$\begin{aligned}(r/L)^{\lambda-1} &= (r/L)^{t-1+ip} = (r/L)^{t-1}\,(r/L)^{ip} \\ &= (r/L)^{t-1}\,\exp(ip\,\ln(r/L)) = (r/L)^{t-1}[\,\cos(p\,\ln(r/L)) + i\sin(p\,\ln(r/L))]\end{aligned} \tag{37}$$

This leads to the stresses

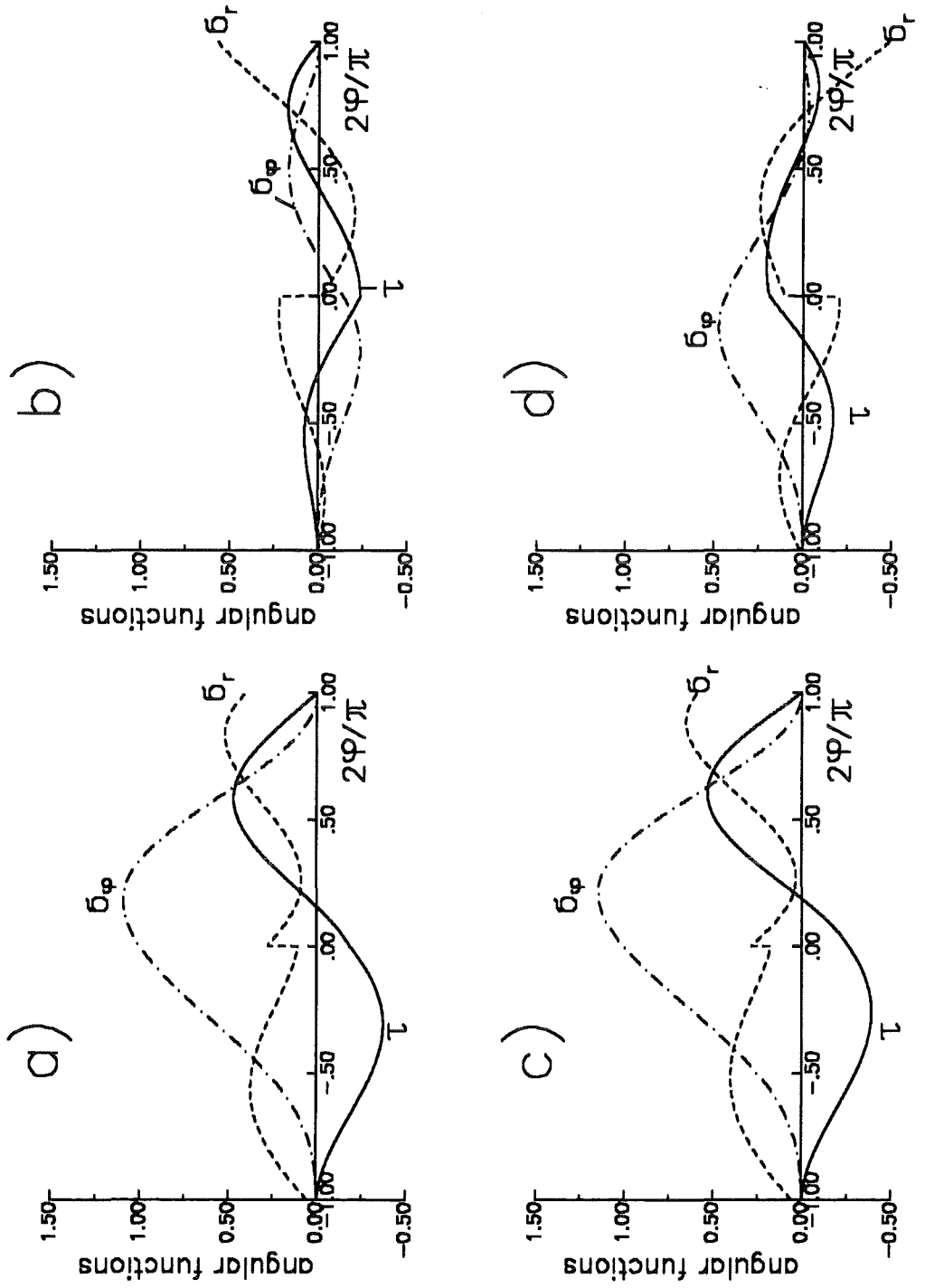

Figure 12. Angular functions. Angular functions for the first non-singular solutions, $t = 1.7563$: a) f^c ($p = 0.4121$), b) f^s ($p = 0.4121$), c) f^c ($p = -0.4121$), d) f^s ($p = -0.4121$).

$$\sigma_r = \sum_{k=0}^{\infty} K_k (r/L)^{t-1} \left\{ \cos[p_k \ln(r/L)]\, f^c_{k,r}(\varphi) + \sin[p_k \ln(r/L)]\, f^s_{k,r}(\varphi) \right\} \tag{38}$$

$$\sigma_\varphi = \sum_{k=0}^{\infty} K_k (r/L)^{t-1} \left\{ \cos[p_k \ln(r/L)]\, f^c_{k,\varphi}(\varphi) + \sin[p_k \ln(r/L)]\, f^s_{k,\varphi}(\varphi) \right\} \tag{39}$$

$$\tau_{r\varphi} = \sum_{k=0}^{\infty} K_k (r/L)^{t-1} \left\{ \cos[p_k \ln(r/L)]\, f^c_{k,r\varphi}(\varphi) + \sin[p_k \ln(r/L)]\, f^s_{k,r\varphi}(\varphi) \right\} \tag{40}$$

The same result was obtained earlier by Yang [5] who applied complex stress functions. In [5] and [17] also the angular functions f^c and f^s are given in analytical form. Figure 12 shows the angular functions for the first zero with $t > 1$. One can see that the angular functions belonging to the sine terms, parts b) and d), are clearly smaller than those belonging to the cosine terms, parts a) and c). This is also the case for higher order solutions as shown in the Appendix. Differences between the angular functions for positive and negative imaginary parts are more significant for the angular functions belonging to the sine terms than for those belonging to the cosine terms. With increasing t the angular functions become more and more oscillating (see Appendix, fig38).

3. Boundary Collocation

3.1 Description of the procedure

The still unknown coefficients K_k of the series representations of stresses are determined by fitting the resulting stresses to the specified boundary conditions at the boundaries, namely constant stresses normal to the upper and lower surfaces and disappering shear stresses along the whole surface. Since the plate investigated features right angles, it is convenient to express the stresses in Cartesian coordinates. From the stress components in polar coordinates the stresses in Cartesian coordinates result as

$$\sigma_x = \sigma_r \cos^2\varphi + \sigma_\varphi \sin^2\varphi - 2\tau_{r\varphi} \sin\varphi \cos\varphi \tag{41}$$

$$\sigma_y = \sigma_r \sin^2\varphi + \sigma_\varphi \cos^2\varphi + 2\tau_{r\varphi} \sin\varphi \cos\varphi \tag{42}$$

$$\tau_{xy} = (\sigma_r - \sigma_\varphi) \sin\varphi \cos\varphi + \tau_{r\varphi}(\cos^2\varphi - \sin^2\varphi) \tag{43}$$

Some of the boundary conditions are automatically fulfilled. It holds for $\varphi = \pi/2$ ($x = 0$)

$$\begin{aligned} \sigma_x &= \sigma_\varphi = 0 \\ \tau_{xy} &= \tau_{r\varphi} = 0 \end{aligned} \tag{44}$$

These conditions were used for determination of the eigenvalues and for computation of the coefficients in the angular functions and will, therefore, not provide information about K_k. The conditions at the opposite boundary are

$$\begin{aligned} \sigma_x &= 0 \quad \text{for} \quad x = 2L \\ \tau_{xy} &= 0 \quad \text{for} \quad x = 2L \end{aligned} \tag{45}$$

In case of the stresses at the lower and upper boundaries it has to be taken into consideration that the plate of dissimilar materials exhibits two equivalent singularities at $y = 0, x = 0$ and $y = 0, x = 2L$. Due to symmetry, the sum of the two normal stress components has to balance the normal tractions and the sum of the two shear stresses has to balance the externally applied shear tractions $\tau_{xy} = 0$, i.e.

$$\sigma_y(x) + \sigma_y(2L - x) = \sigma_{appl} \quad \text{for} \quad y = \pm H$$
$$\tau_{xy}(x) - \tau_{xy}(2L - x) = 0 \quad \text{for} \quad y = \pm H \tag{46}$$

where σ_{appl} are the externally applied tractions at the upper and lower bounds of the plate (see fig.1). For the evaluation of the series expansions of stresses we have to truncate the infinite series after N terms. If for a selected number of $(N+1)$ edge points the related stress components are known, we obtain a system of $2(N+1)$ equations with $2(N+1)$ unknowns whose solutions allow all $2(N+1)$ coefficients K_k to be determined.
The expenditure in terms of computation can be reduced by selection of a rather large number of edge points and by solving subsequently the then overdetermined system of equations using the least squares of deviations so that a set of "best" coefficients are obtained. The Harwell subroutine V02AD is used here to determine the best fit. The number of fitting nodes has been chosen to be $2N$ and the number of equations consequently is $M = 4N$. A function S^2 is defined by

$$S^2 = \sum_{(M)} [(\sigma_y - \sigma_{appl})^2 + \tau_{xy}^2] \tag{47}$$

which represents the square sum of deviations between the eigenfunction solution and the prescribed boundary tractions.
The fitting points have been selected to have continuous angles φ, i.e. the n-th point has the polar angle

$$\varphi_n = \frac{\pi}{2N}\, n - \frac{\pi}{2} \tag{48}$$

3.2 Results

3.2.1 Accuracy and Convergence

First materials with conjugate complex eigenvalues are considered. The material parameters were chosen as given by data set A, eq.(16). In the following considerations plane stress conditions will be chosen. Figure 13 represents the first coefficient (belonging to the singular stresses) as a function of the number of series terms used. As this value is proportional to the applied stress (denoted just σ below), the coefficient is normalised to this stress value. The result converges to $K/\sigma = 0.6875 \pm 0.001$ for $N \geq 100$.
Figure 14 represents the least-squares sum of stresses at the circumference after application of the least-squares routine to the special case of the applied stress chosen to be $\sigma_{appl} = 1$.
The sum of squares becomes very small for $N \geq 100$ and S^2 is on the order of $S^2 < 1 \cdot 10^{-6}$ from which a mean deviation

$$\delta = \sqrt{\frac{S^2}{M}} < 5 \cdot 10^{-5} \tag{49}$$

results.

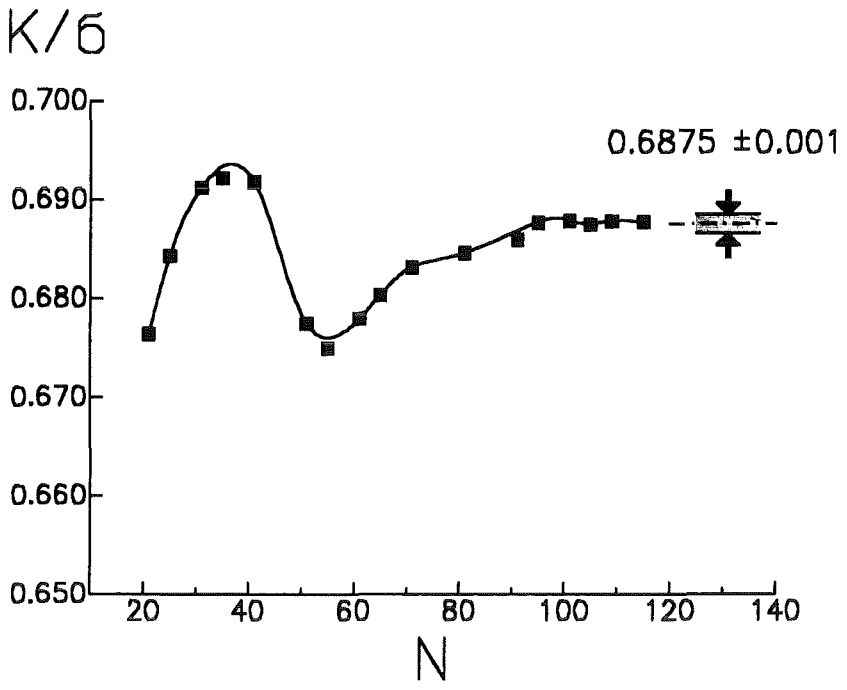

Figure 13. BCM-procedure. Convergence of the Boundary Collocation Method (BCM) for an increased number of terms used in the Airy stress function (data: $E_2/E_1 = 10$, $\nu_1 = \nu_2 = 0.3$, $H/L = 2.3$).

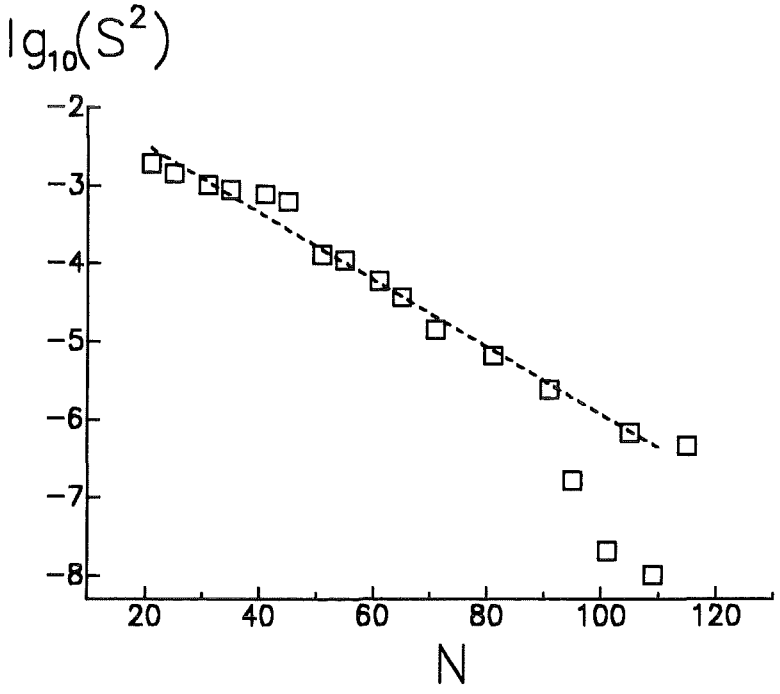

Figure 14. BCM-procedure. Sum of squares for a number of $M = 4N$ equations (data as given in fig.13).

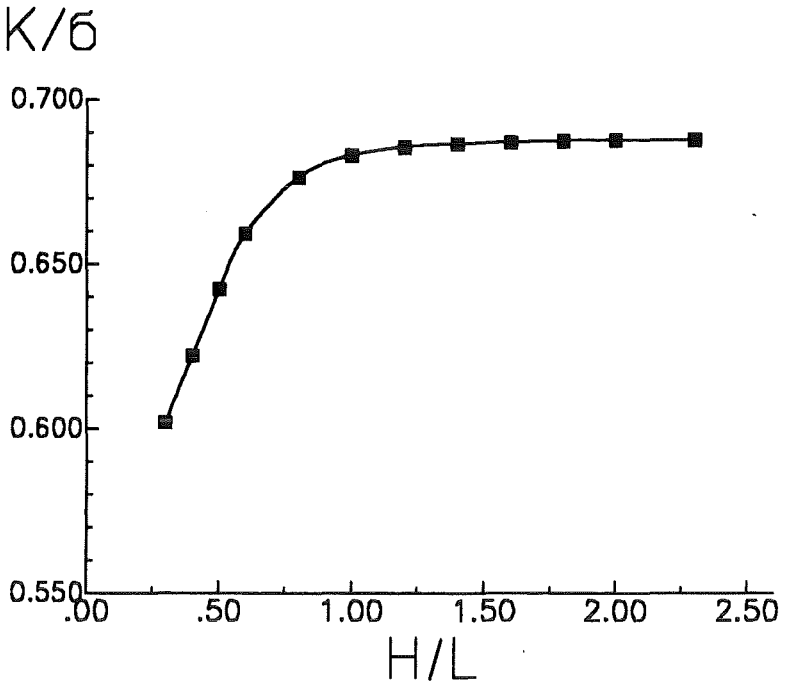

Figure 15. Influence of geometry. Influence of the specimen height on the ratio K/σ.

The influence of the height H of the plate on the stress intensity factor K is shown in fig.15. It is obvious that for $H/L \geq 2$ the stress intensity factor is independent of the plate height. For the further calculations the value $H/L = 2.3$ was used which sufficiently represents an infinite plate. The next two terms are represented in normalised form in the Appendix (fig.37). The specimen height has also an influence on the stress intensity factor for the case that the load is not homogeneously distributed along the ends of the plate. This will be shown in Section 4 (see e.g. fig.36). We can conclude that for a specimen height $H/L > 2$ the stress intensity factor is nearly independent of the special stress distribution but will be affected only by the mean value in accordance with Saint Venant's theorem.

3.2.2 Stress intensity factors for one single stress exponent $\omega = 0$ ($\nu_1 = \nu_2$)

If the two materials have identical Poisson ratios, $\nu_1 = \nu_2$, only one stress exponent ω can be reached by variation of the ratio E_2/E_1. Introducing $\nu_1 = \nu_2$ into eqs.(13) and (14) gives, with $m_1 = m_2 = m$,

$$\beta = \frac{m-2}{m}\alpha \quad , \tag{50}$$

i.e. all possible combinations in the $\alpha - \beta$ diagram are located on straight lines through the origin where $\omega = 0$ is reached. The stress intensity factor for the singular stress term was computed for different Young's moduli and several values of Poisson ratios assuming plane stress conditions. For these calculations $N = 100$ and $H/L = 2.3$ were used. The results are plotted in fig.16 as a function of the singularity exponent ω. The data points related to the same Poisson ratio are connected by curves. The insert in

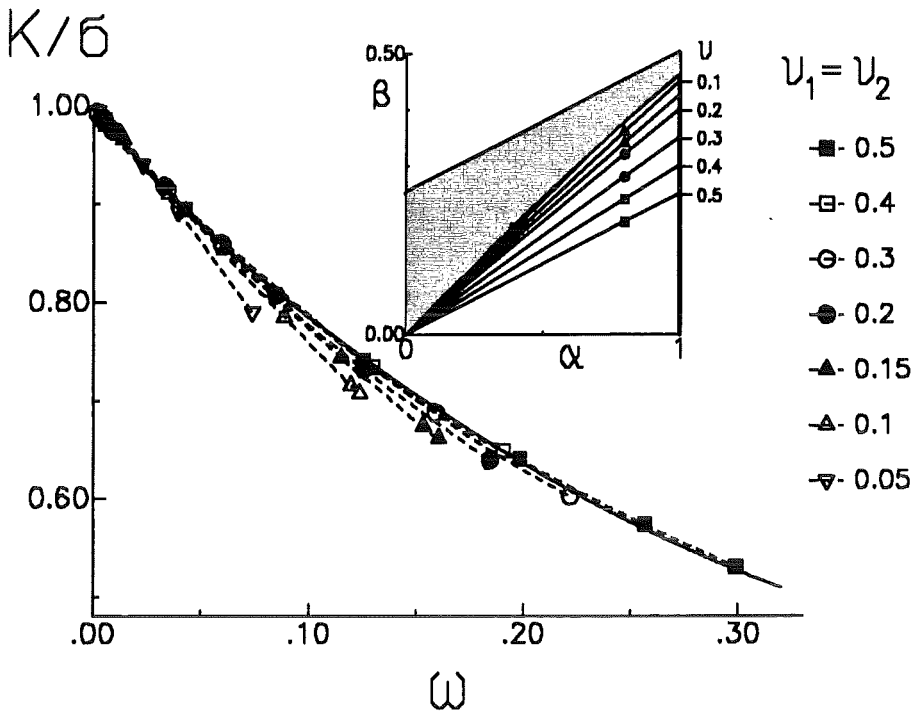

Figure 16. Stress intensity factor. Ratio K/σ as a function of the singularity exponent ω for several Poisson ratios $\nu_1 = \nu_2$. Solid line: approximation proposed by Yang [5], eq.(51).

fig.16 describes the related $\alpha - \beta$ dependencies. The BCM-results are compared with a fit-formula proposed by Yang [5]

$$K/\sigma = 1 - 2.89\omega + 11.4\omega^2 - 51.9\omega^3 + 135.7\omega^4 - 135.8\omega^5 \qquad (51)$$

This relation is entered in fig.16 as solid curve. Especially in the cases $\nu_1 = \nu_2 =$ 0.3,0.4 and 0.5 this relation fits the BCM-data very well. In order to eliminate the remaining small deviations the data points of fig.16 were shifted by $0.0235\alpha^6$. The result is plotted in fig.17 with one data point - $\omega = 0.074$, $K/\sigma = 0.79$, $\nu_1 = \nu_2 = 0.05$ - from the region $\alpha/2 < \beta < \alpha/2 - 0.0384\alpha^{2.2}$ excluded. This figure gives rise to an improved fit-relation

$$K/\sigma = \exp(-2.45\omega(1.1 - \omega)) - 0.0235\alpha^6 \qquad (52)$$

which is entered in fig.17 as solid line.

3.2.3 Stress intensity factors in case of two solutions $\omega = 0$

If the two materials exhibit different Poisson ratios, one has to expect two different material combinations with $\omega = 0$. This can be readily concluded from fig.18. In the Dundurs plot one obtains straight lines which (in the case $\nu_1 \neq \nu_2$) intersect the curves $\beta = \alpha/2$ as well as the ordinate $\alpha = 0$. At both intersections the value $\omega = 0$ is reached. Since in both cases different α and different β values occur one has to expect different values of K/σ at $\omega = 0$.

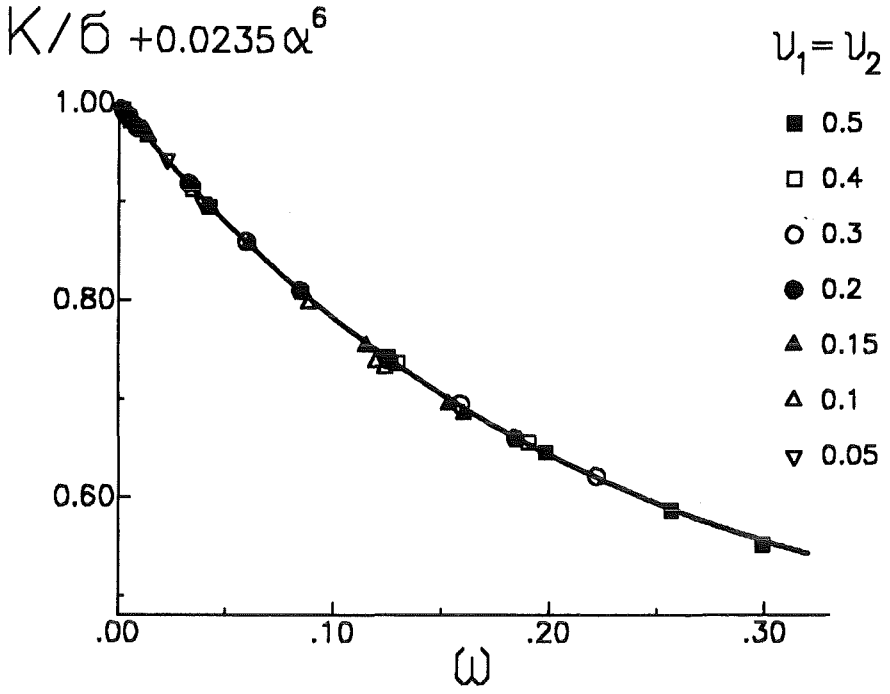

Figure 17. Stress intensity factor. Elimination of the influence of the Dundurs parameter α by shifting the single data of fig.16 (with data from $\alpha/2 < \beta < \alpha/2 - 0.0384\alpha^{2.2}$ excluded) by the amount $0.0235\alpha^6$. Comparison of the numerical data (symbols) with the fit-relation, eq.(52) (curve).

BCM computations were performed with the combinations of Poisson ratios: ($\nu_1 = 0.15$, $\nu_2 = 0.45$), ($\nu_1 = 0.2$, $\nu_2 = 0.4$), ($\nu_1 = 0.3$, $\nu_2 = 0.3$), and ($\nu_1 = 0.4$, $\nu_2 = 0.2$). The results are shown in fig.19. A comparison with the formula proposed by Yang [5], eq.(51), is given in fig.20. Also in this case, we find good agreement for the combinations $\nu_1 = 0.3$, $\nu_2 = 0.3$ and $\nu_1 = 0.4$, $\nu_2 = 0.2$. After shifting the single data by an amount of $0.0235\alpha^6$ the representation in fig.21 is obtained. Also in this case, the single data nearly coincide with the solid curve. Having in mind that for $\omega = 0$ two different stress intensity factors will occur one should not apply the approximate relations for $\omega = 0$.
In case of thermal loadings Tilscher et al. [18] found that the relation $K/\sigma_0 = f(\omega)$ significantly deviates from a unique function for $\omega \simeq 0$ and for negative ω. This effect has also to be expected for mechanical loading. BCM-computations were carried out with strongly different Poisson ratios. In fig.22 results are shown for $\nu_1 = 0.01$ and $\nu_2 = 0.49$ and different E_2/E_1-ratios. The data points show the expected non-unique $K/\sigma_0 = f(\omega)$ relation. The insert represents the variation of the Dundurs parameters. Figure 23 represents the curve in detail for $\omega < 0$. In fig.24 results obtained for $\nu_1 = 0.10$ and $\nu_2 = 0.50$ are shown. Also in this case the deviations from a unique K/σ vs. ω relation are evident, but less pronounced than in fig.22. Finally, in figs.25 and 26, the normalised stress intensity factors are plotted in Dundurs diagrams.

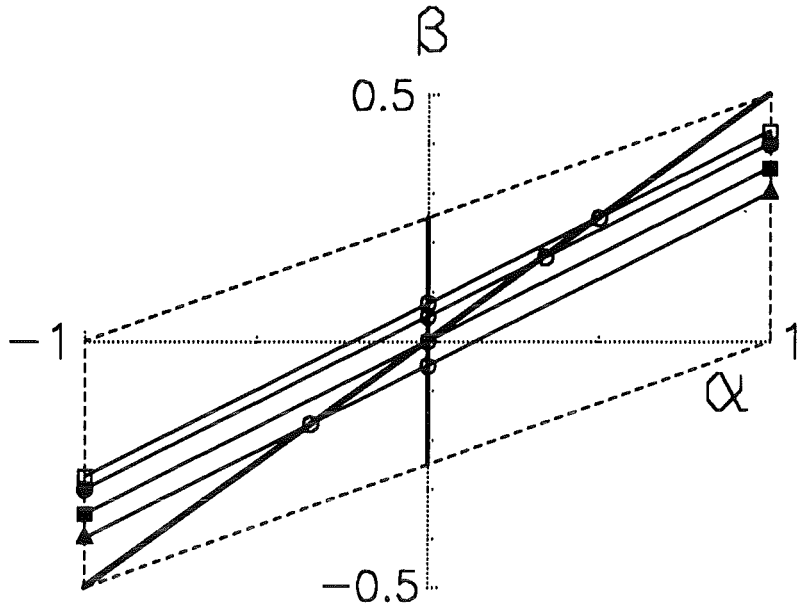

Figure 18. Dundurs parameter. Dundurs plot of material combinations with differently chosen Poisson ratios. The symbols at the line ends correspond to the symbols used in fig.19. The open circles represent $\omega = 0$.

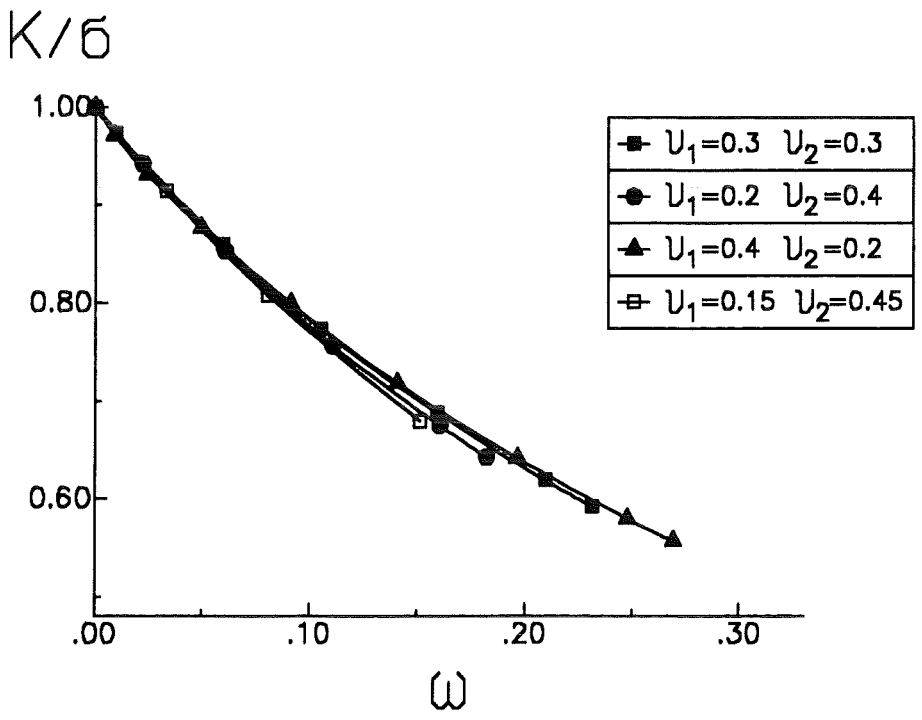

Figure 19. Stress intensity factor. Ratio K/σ as a function of the singularity exponent ω for different Poisson ratios.

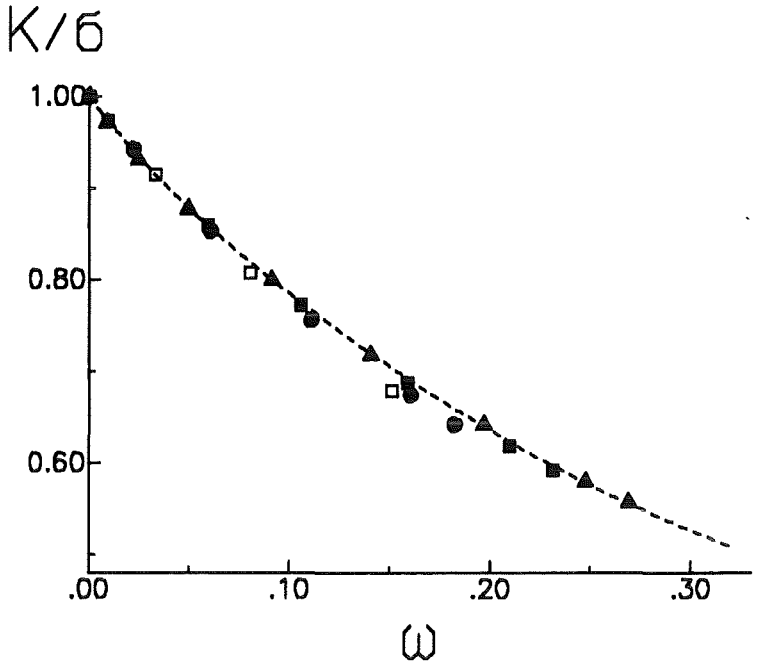

Figure 20. Stress intensity factor. Results of fig.19 (symbols) compared with a fit-relation proposed by Yang [5], eq.(51), (dashed curve).

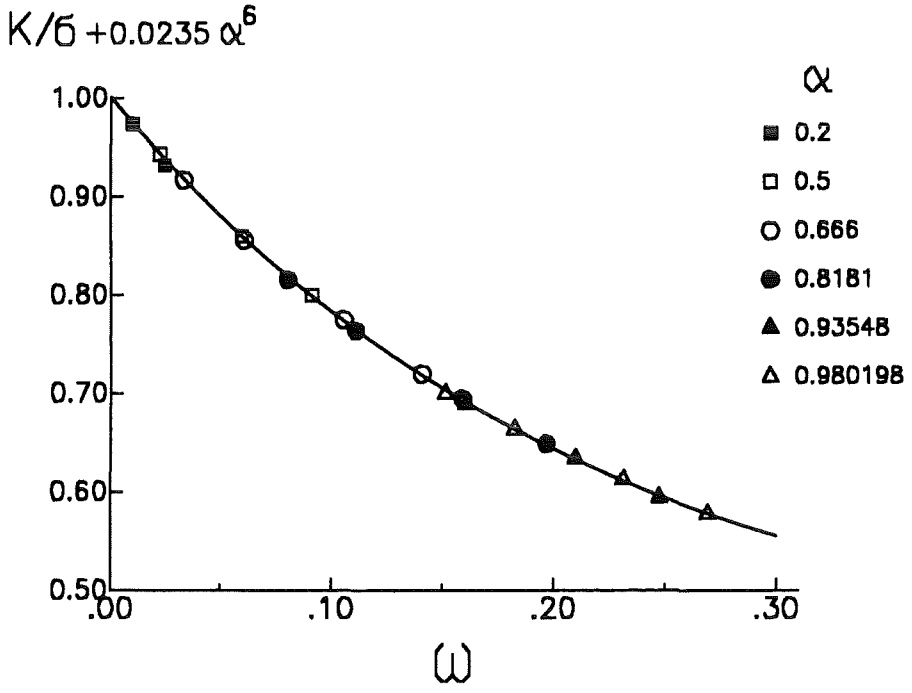

Figure 21. Stress intensity factor relation. Elimination of the influence of the Dundurs parameter α by shifting the single curves of fig.19 by the amount $0.0235\alpha^6$. Comparison of the numerical data (symbols) with the fit-relation eq.(52) (curve).

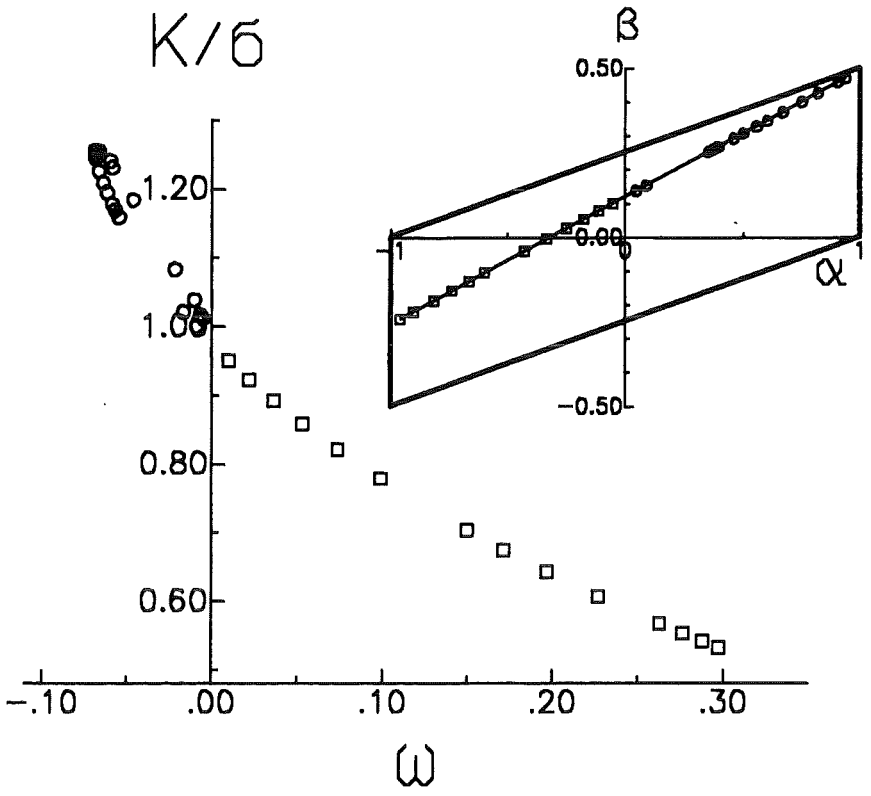

Figure 22. Stress intensity factor relation. Stress intensity factor including negative ω-values ($\nu_1 = 0.01$, $\nu_2 = 0.49$). Insert: Variation of the Dundurs parameters.

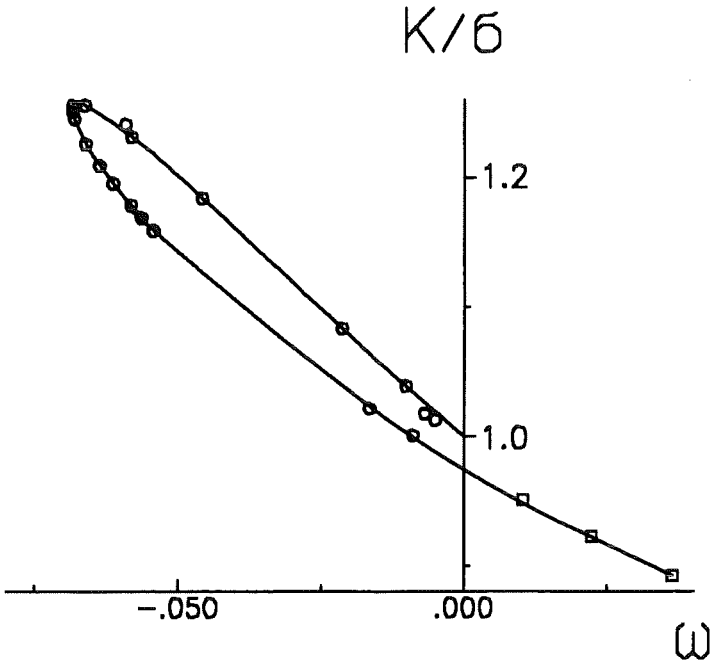

Figure 23. Stress intensity factor relation. Detail of fig.22.

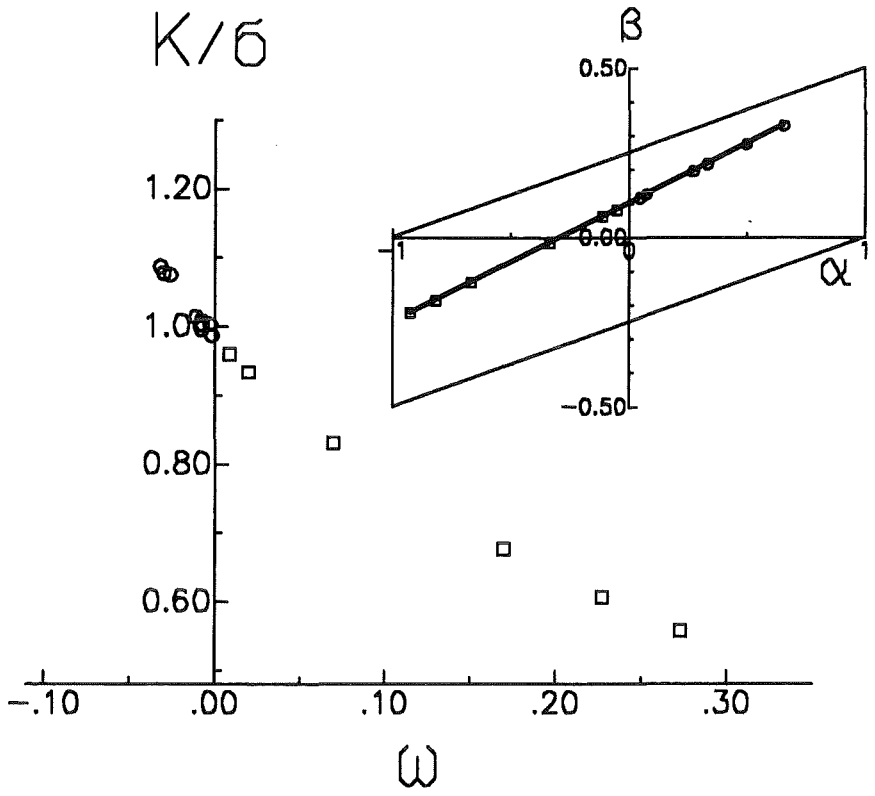

Figure 24. Stress intensity factor relation. Stress intensity factor including negative ω-values ($\nu_1 = 0.10$, $\nu_2 = 0.50$). Insert: Variation of the Dundurs parameters.

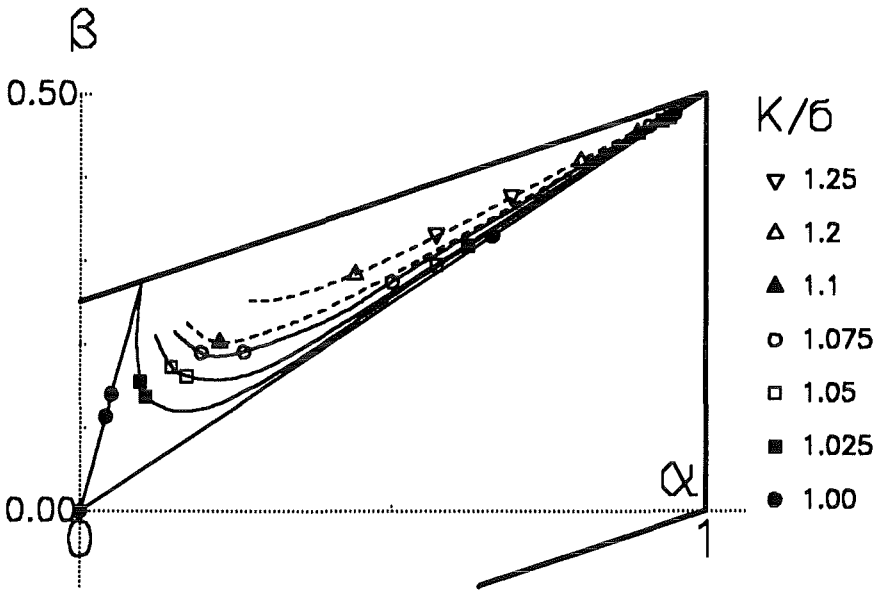

Figure 25. Dundurs diagram for stress intensity factors. Stress intensity factor for $\omega \leq 0$.

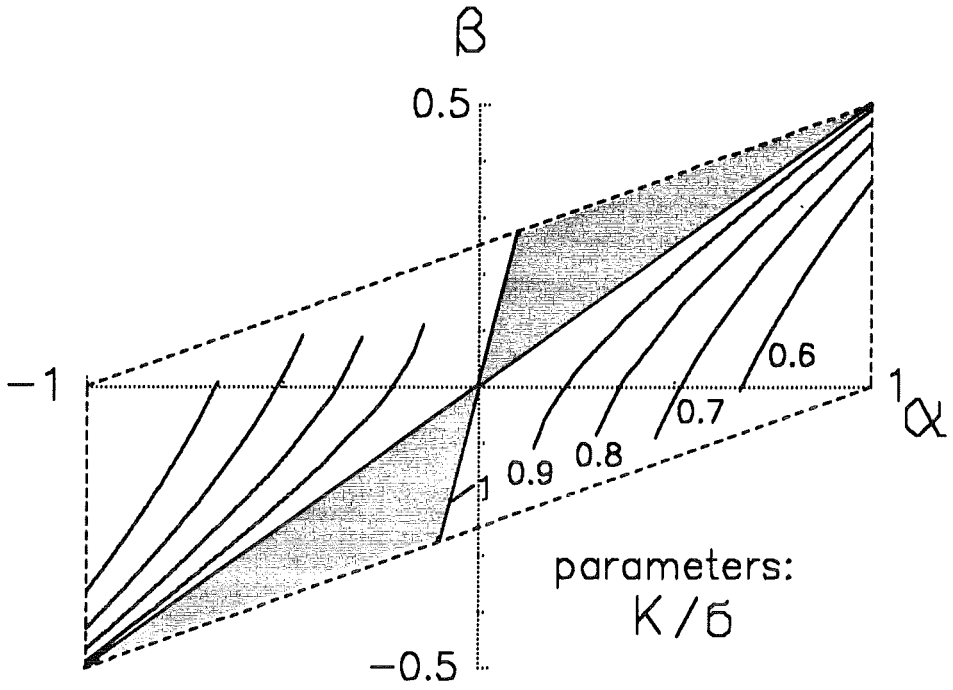

Figure 26. Dundurs diagram for stress intensity factors. Stress intensity factor for $\omega \geq 0$.

3.3 Influence of the plate length on the stress intensity factor

3.3.1 Pure tension and bending

The two mechanical loadings of highest importance are pure tension with $\sigma(x) = \sigma_0$ and pure bending with

$$\sigma(x) = \sigma_0(1 - x/L) \tag{53}$$

The related stress intensity factors are shown in fig.27.

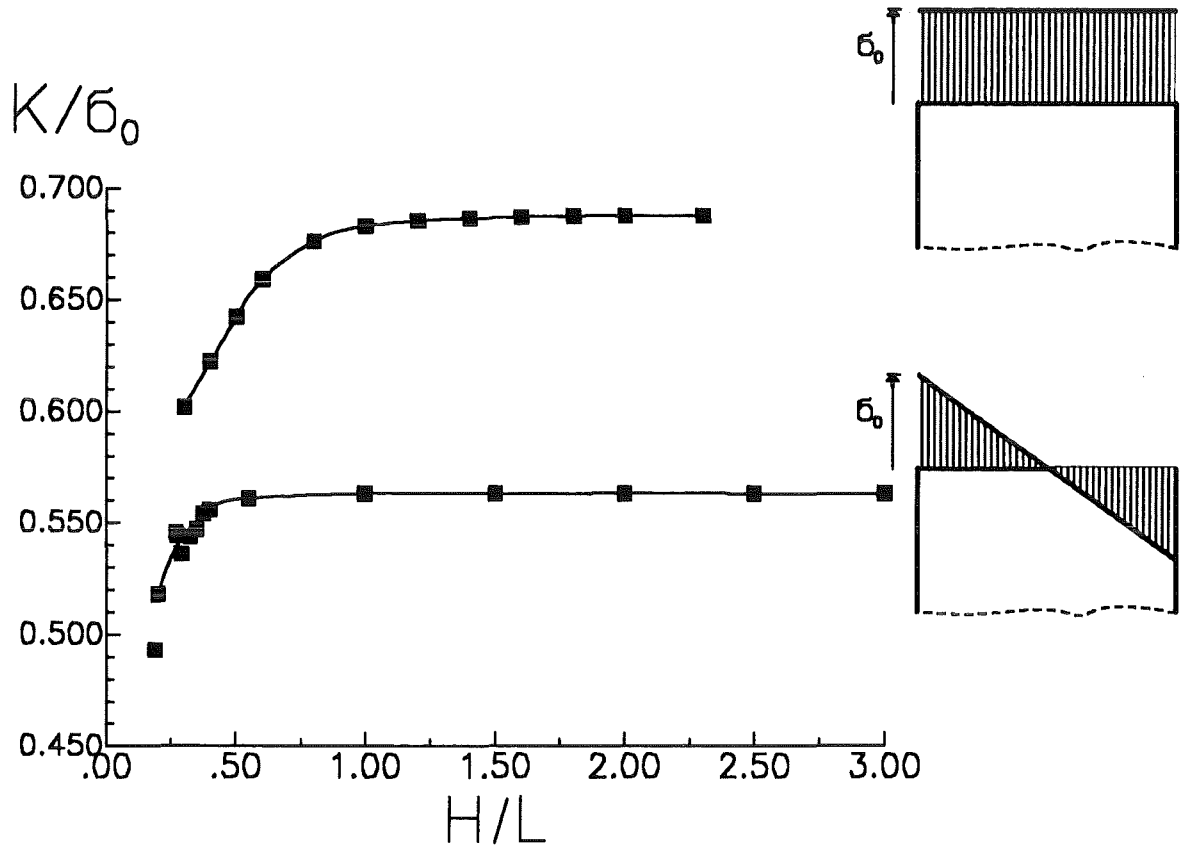

Figure 27. Tension and bending. Plate with linear external tractions; stress intensity factor for pure bending (lower curve) compared with pure tension (upper curve). In case of bending σ_0 is the outer fibre stress. Data set A, eq.(28).

Figure 27 makes obvious that pure tension exhibits significantly higher stress intensity factors than bending.

3.3.1.1 Symmetrical tractions

Symmetrical tractions are defined by

$$\sigma(x) = \sigma(2L - x) \tag{54}$$

In fig.28 the special stress distribution

$$\sigma(x) = \sigma_0 \sin(\pi x/2L) \tag{55}$$

was chosen. Figure 28 is a comparison of the solutions for sinusoidal with constant tractions.

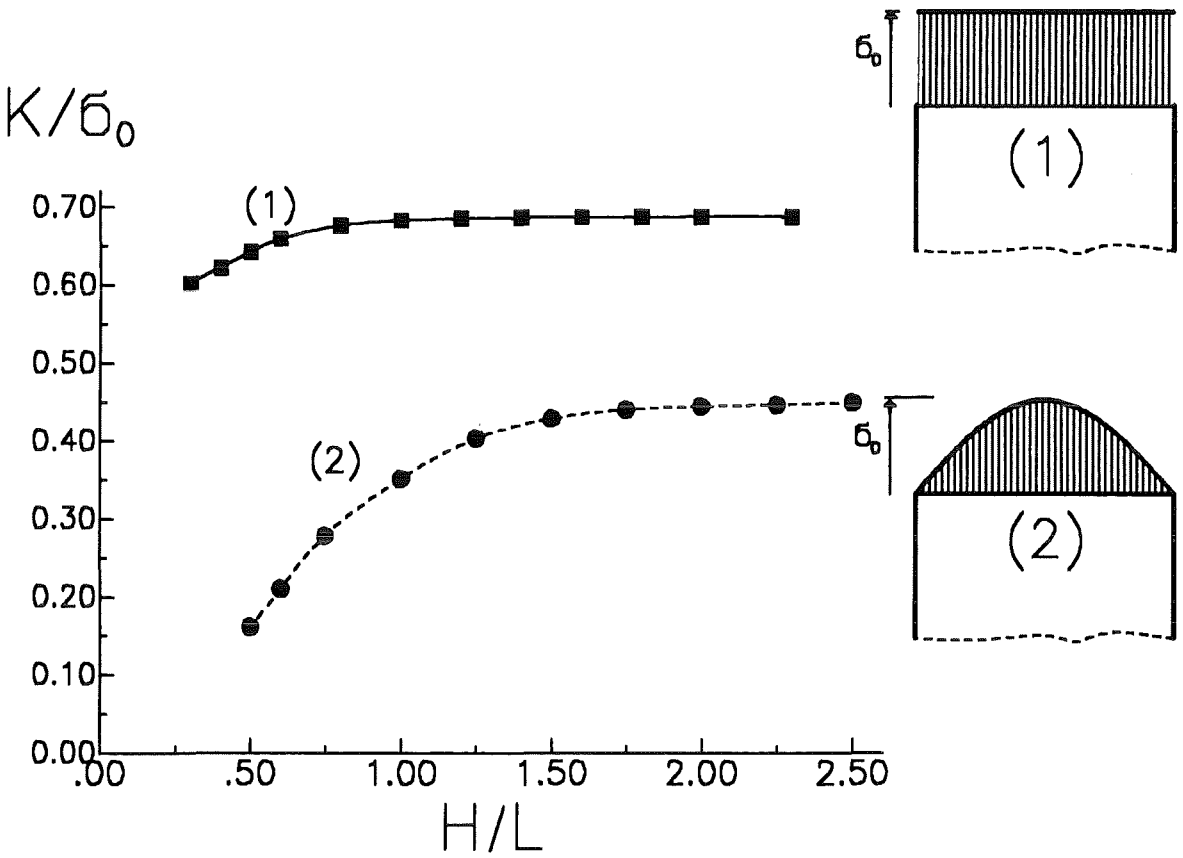

Figure 28. Symmetrical loading. Plate with sinusoidal-shaped external tractions (upper curve) compared with pure bending stresses (lower curve). Data set A, eq.(28).

In fig.29 the stress intensity factors are normalised to the averaged stresses, i.e. $\overline{\sigma} = \sigma_0$ for constant stress and

$$\bar{\sigma} = \frac{2}{\pi}\sigma_0 \tag{56}$$

for the sinusoidal distribution. In this normalisation we see that the two solutions are nearly identical for $H/L > 1.5$, with maximum deviations of about 1%.

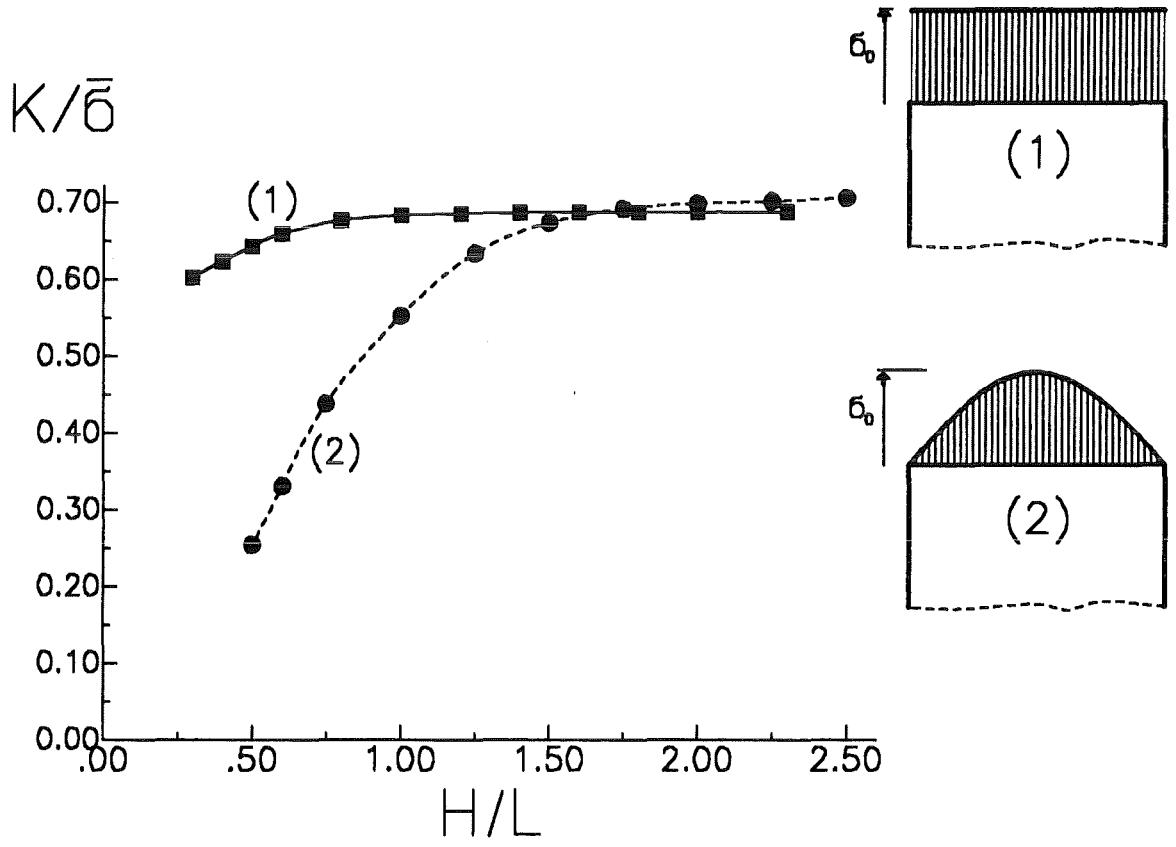

Figure 29. Symmetrical loading. Results of fig.29 normalised to the average stress $\bar{\sigma}$.

3.3.1.2 Antisymmetrical tractions

Antisymmetrical tractions are defined by

$$\sigma(x) = -\sigma(2L - x) \tag{57}$$

In fig.30 the tractions are

$$\sigma(x) = \sigma_0 \cos(\pi x/2L) \tag{58}$$

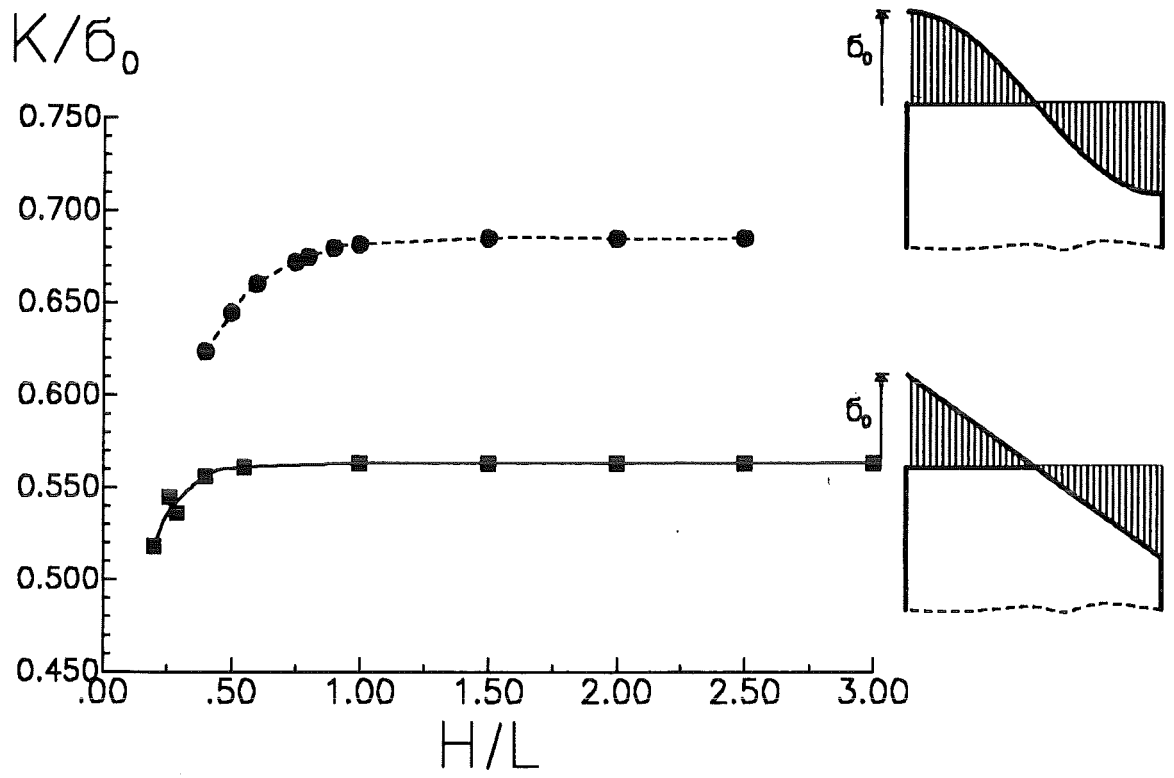

Figure 30. Antisymmetrical loading. Cosinusoidal-shaped external tractions compared with pure bending. Data set A, eq.(28).

We normalise the outer fibre stress in such a way that the bending moment becomes identical for the two types of traction, i.e. for the cosine-shaped tractions

$$\sigma_{0,\,eff} = \frac{12}{\pi^2}\,\sigma_0 \tag{59}$$

Then one obtains the curves represented in fig.31. From this representation we conclude that for $H/L > 1.25$ both curves coincide totally.

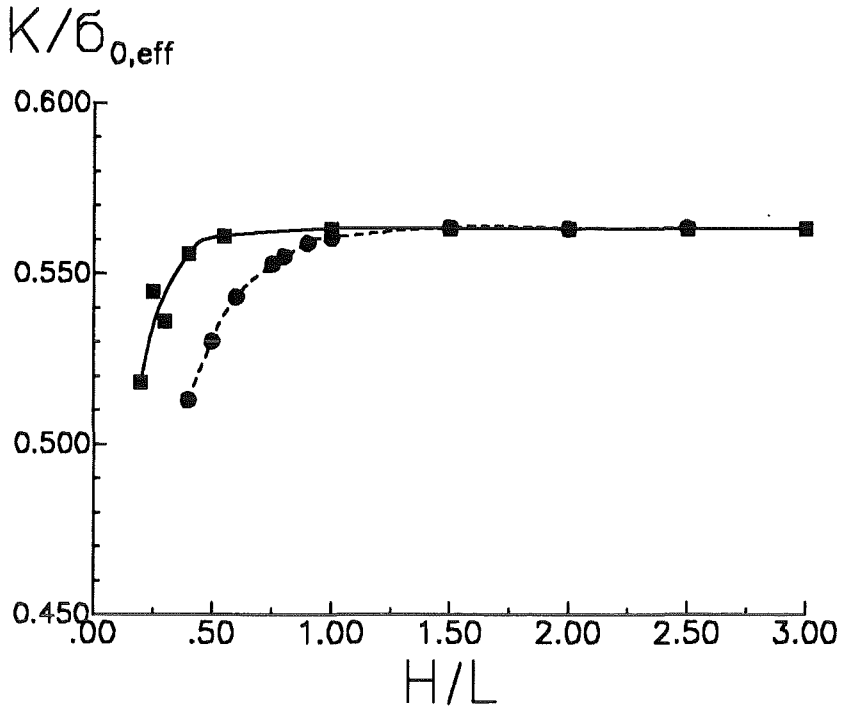

Figure 31. Antisymmetrical loading. Stress intensity factors according to fig.30; stress intensity factor normalised to the same effective outer fibre stress (yielding identical bending moments).

3.3.2 Tractions with disappearing normal forces and bending moments

It has to be expected from the theorem of Saint Venant that for large values of H/L the effect of any stress distribution applied at the plate ends reduces to the effect caused by the normal force and by the bending moment. This result is, in principle, already obvious from figs.29 and 31. These figures lead to application of tractions with disappearing mean value and disappearing bending moment. This can be done by selecting a symmetrical stress distribution ($M = 0$) and application of the difference between an arbitrary stress (here sinusoidal) and its mean value, i.e. by

$$\sigma(x) = \sigma_0 \left[\sin\left(\frac{x}{L} \frac{\pi}{2} \right) - \frac{2}{\pi} \right] \tag{60}$$

(see fig.32)

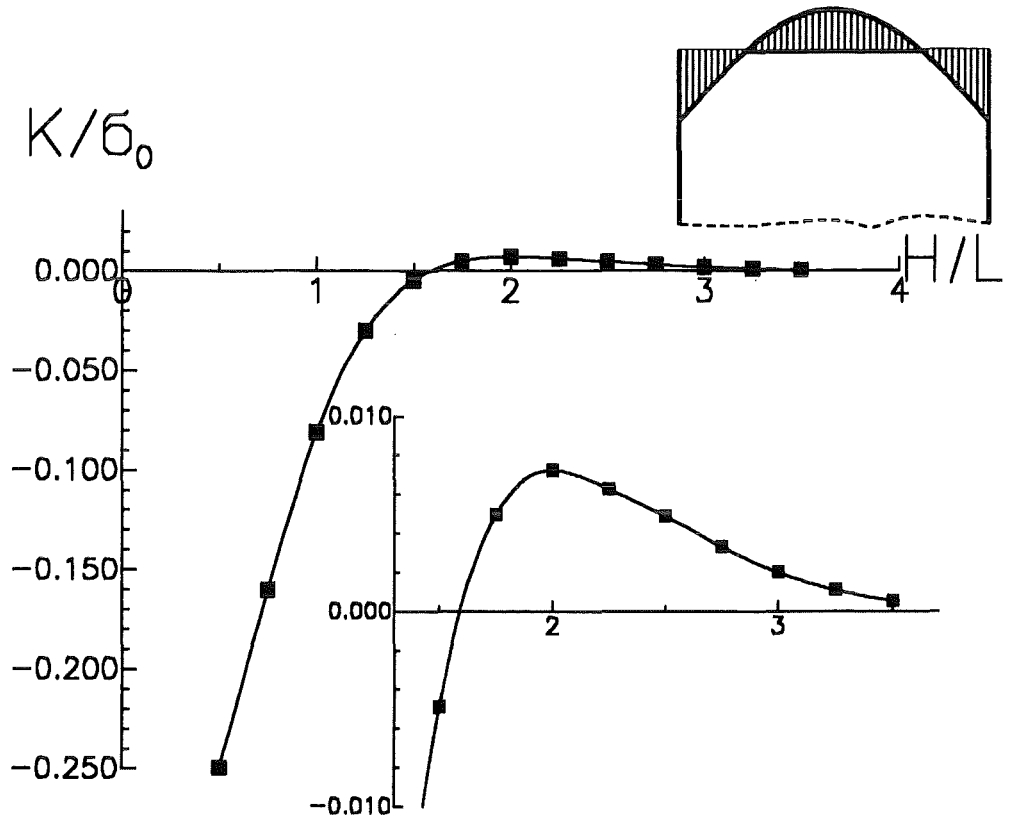

Figure 32. Symmetrical loading. Plate with sinusoidal-shaped external tractions and disappearing resultant according to eq.(60).

or by application of an arbitrary antisymmetric stress ($\overline{\sigma} = 0$) which generates the same bending moment as the linear stress distribution, i.e. by

$$\sigma(x) = \sigma_0 \left[\cos\left(\frac{x}{L} \frac{\pi}{2} \right) - \frac{12}{\pi^2} \left(1 - \frac{x}{L} \right) \right] \tag{61}$$

(see fig.33)

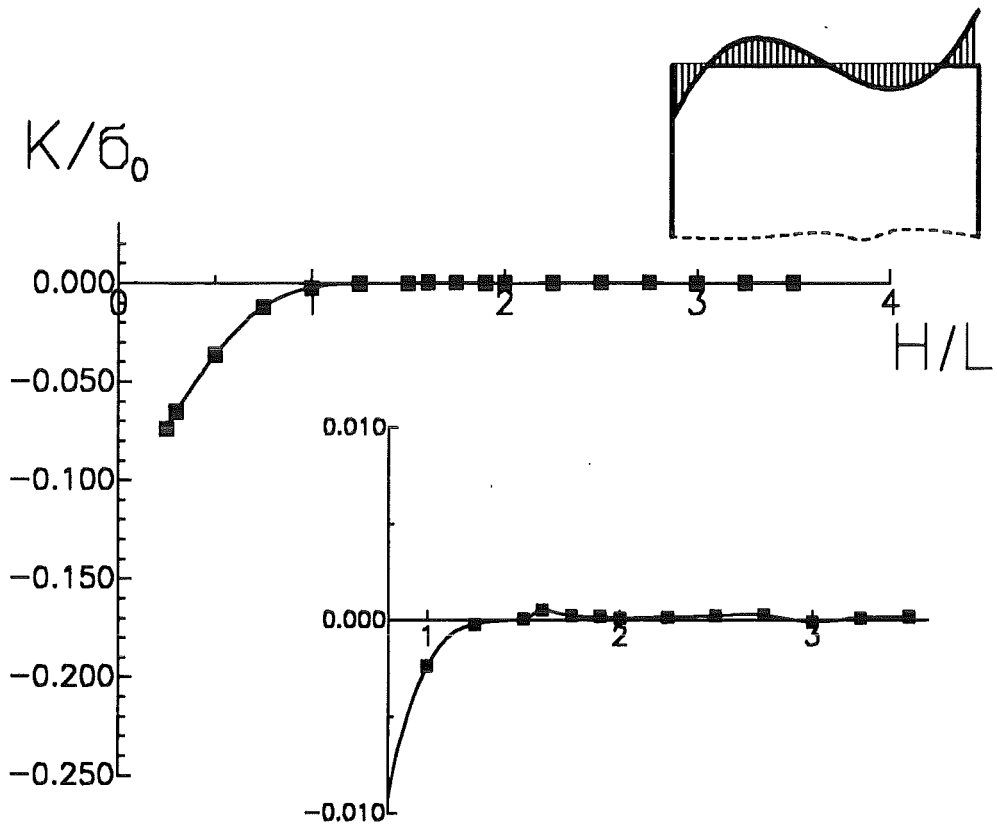

Figure 33. Antisymmetrical loading. Antisymmetrical tractions; cosinusoidal-shaped external stresses with disappearing bending moment according to eq.(61).

In the two last examples the theorem of Saint Venant could be checked with very high accuracy. The sensitivity is very high since the result is not concluded from the difference of two numerically obtained results with cumulated error margins.
In order to show the influence of the singularity exponent ω on the stress intensity factor, the computations represented in fig.32 were repeated for the same Poisson ratios $\nu_1 = \nu_2 = 0.3$ but different ratios E_1/E_2 which resulted in different ω-values. The result is plotted in fig.34. We can conclude that for $H/L > 3.6$ the limit case of a strip of infinite height is sufficiently fulfilled for all ω. The tendency becomes obvious that the stress intensity factor disappears earlier with increasing ω.

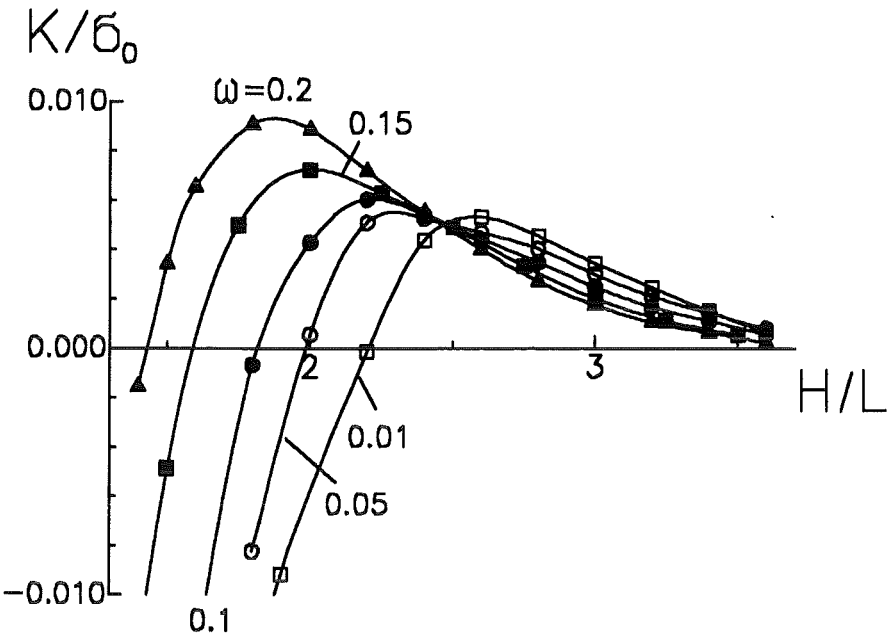

Figure 34. Symmetrical loading. Influence of the singularity exponent ω on the stress intensity factor for the same loading as used in fig.32.

3.3.3 Other non-homogeneous symmetric loadings

Different tractions at the upper and the lower boundaries of the plate are chosen in fig.35 which lead to the same resulting normal forces. In fig.36 the stress intensity factors are compared with the case of homogeneously distributed tractions. Also in this case we obtain identical stress intensity factors for $H/L > 2$.

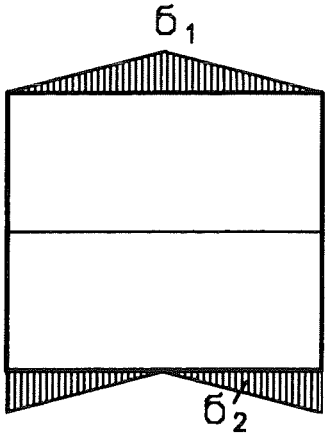

Figure 35. Non-symmetry to the interface. Plate with two non-homogeneously distributed externally applied tractions.

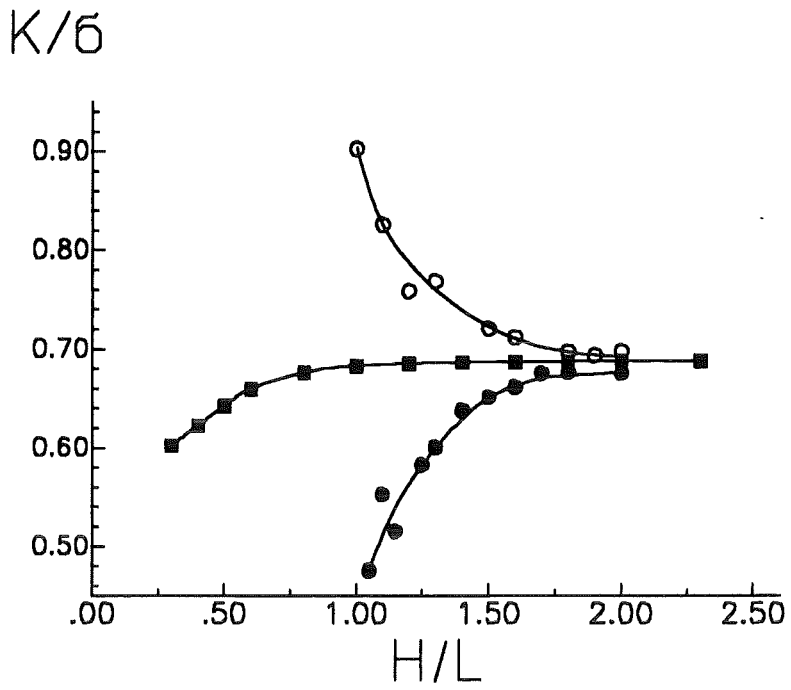

Figure 36. Non-symmetry to the interface. Stress intensity factors for the stress distributions illustrated in fig.35. Solid circles: distribution σ_1; open circles: distribution σ_2; squares: constant stress $(\sigma_1 + \sigma_2)$. In K/σ always the mean stress, averaged over $2L$, was introduced. Data set A, eq.(28).

4. References

[1] M.L. Williams, Stress singularities resulting from various boundary conditions in angular corners of plates in extension, J. Appl. Mech., **19**(1952), 526-528.

[2] D.B. Bogy, The edge-bonded elastic wedges of different materials and wedge angles under surface tractions, Trans. ASME J. Appl. Mech., **38**(1971), 377-386.

[3] V.L. Hein, F. Erdogan, Stress singularities in a two-material wedge, Int. J. Fract. **7**(1971) 317-330.

[4] K. Mizuno, K. Miyazawa, T. Suga, Characterization of thermal stress in ceramic/ metal-joints, J. of the Faculty of Engineering, The Univ. of Tokyo (B) Vol. XXXIX, No.4, 1988.

[5] Y.Y. Yang, Spannungssingularitäten in Zweistoffverbunden bei mechanischer und thermischer Belastung, Fortschritt-Berichte VDI, Reihe 18 Nr.113, VDI-Verlag, Düsseldorf, 1992.

[6] D. Munz, Y.Y. Yang, Stress singularities at the interface in bonded dissimilar materials under mechanical and thermal loading, Trans. ASME J. Appl. Mech. **59**(1992) 857-861.

[7] M. Tilscher, D. Munz, Y.Y. Yang, The stress intensity factor in bonded quater planes after a change in temperature, J. Adhesion **49**(1995), 1-21.

[8] M. Heinzelmann, D. Munz, Y.Y. Yang, Computational Mater. Sci. **1**(1993), 259. Adhesion **49**(1995), 1-21.

[9] J.P. Blanchard, N.M. Ghoniem, An eigenfunction approach to singular thermal stresses in bonded strips, J. of Therm. Stresses **12**(1989), 501-527.

[10] J.P. Blanchard, N.M. Ghoniem, Analysis of singular stress fields in duplex components, J. of Nucl. Materials **172**(1990), 54-70.

[11] T. Fett, Determination of stresses in a plate strip of bonded dissimilar materials, Engng. Fract. Mech. **47**(1994), 547-557.

[12] L. Banks-Sills, Y.Y. Yang, D. Munz, A weight function method for determining stress intensity factors of notched homogeneous and bimaterial bodies, in progress.

[13] O. Iancu, Berechnung von thermischen Eigenspannungen in Keramik/ Metall-Verbunden, Fortschritt-Berichte VDI, Reihe 18, Nr. 74, VDI-Verlag, Düsseldorf 1989.

[14] D. Munz, T. Fett, Y.Y. Yang, The regular stress term in bonded dissimilar materials after a change in temperature, Engng. Fract. Mech. **44**(1993), 185-194.

[15] C.B. Biezeno, R. Grammel, Technische Dynamik, Vol.1, Springer-Verlag, Berlin 1953.

[16] M. Tilscher, unpublished results.

[17] Y.Y. Yang, D. Munz, Stress distribution in a dissimilar materials joint for complex singular eigenvalues under thermal loading, J. of Thermal Stresses **18**(1995), 407-419.

[18] M. Tilscher, D. Munz, Y.Y. Yang, The relationship between the stress intensity factor and the stress exponent for bimaterials under thermal loading, Int. Fract. Mech. **65**(1994), R23-R28.

5. Appendix

5.1 Higher order stress intensity factors and angular functions

In the following figures

- the influence of the plate length H on the two first non-singular terms of the Airy stress function is demonstrated (fig.37);
- the oscillating behaviour for higher order stress function terms is shown (fig.38).

The material parameters for figs.37 and 38 are given by data set A, eq.(28).

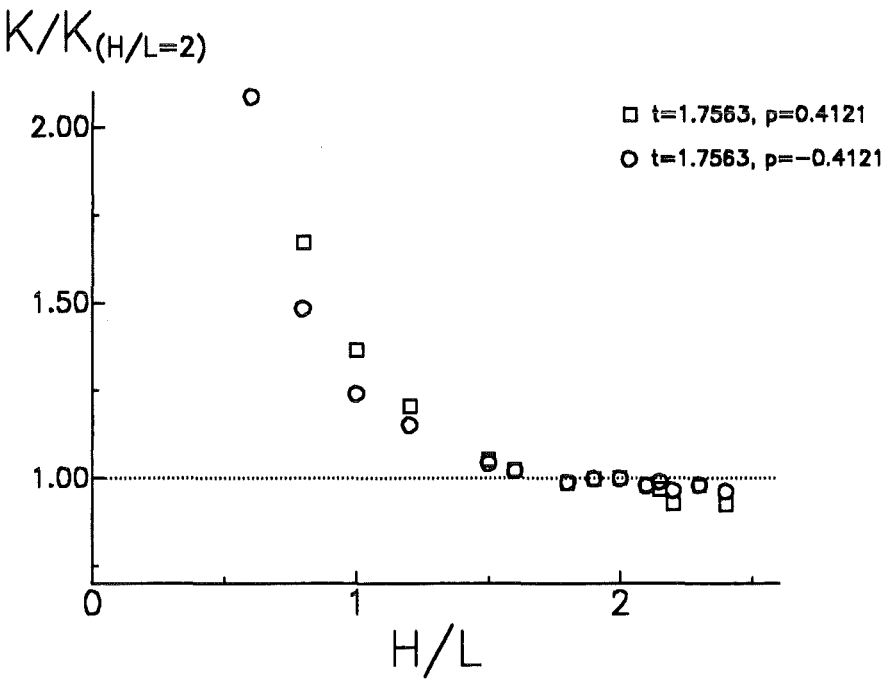

Figure 37. Stress intensity factors for higher order terms. First non-singular solutions. Stress intensity factors normalised to the values at $H/L = 2$. Compared with the singular stress intensity factor term, the "scatter" of the data points increases with increasing eigenvalue.

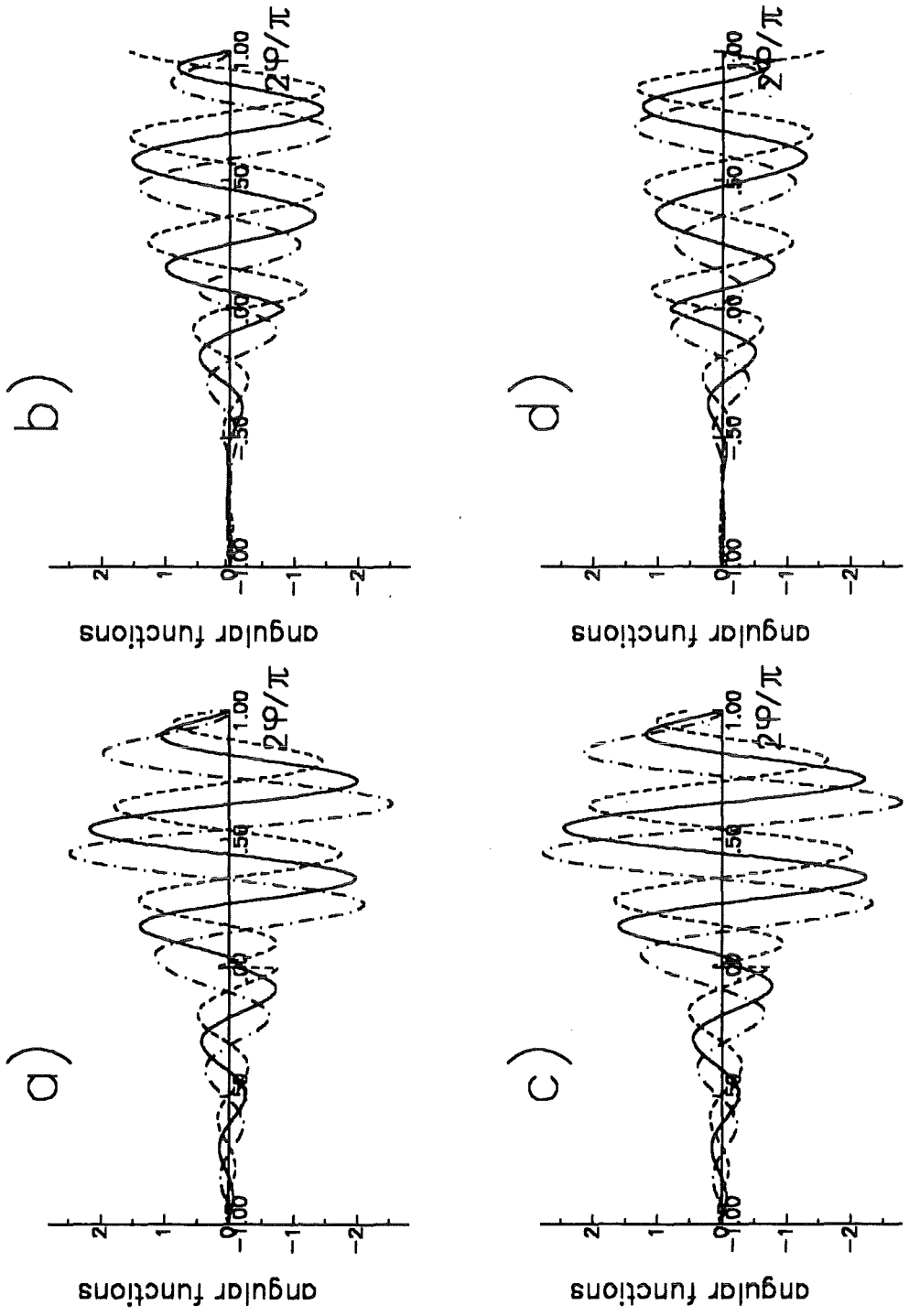

Figure 38. Higher order angular functions. Higher order (non-singular) solutions, $t = 9.8452$: a) f^c ($p = 1.6239$), b) f^s ($p = 1.6239$), c) f^c ($p = -1.6239$), d) f^s ($p = -1.6239$). Dashed lines: radial stress, dash-dotted lines: tangential stress, solid lines: shear stress.

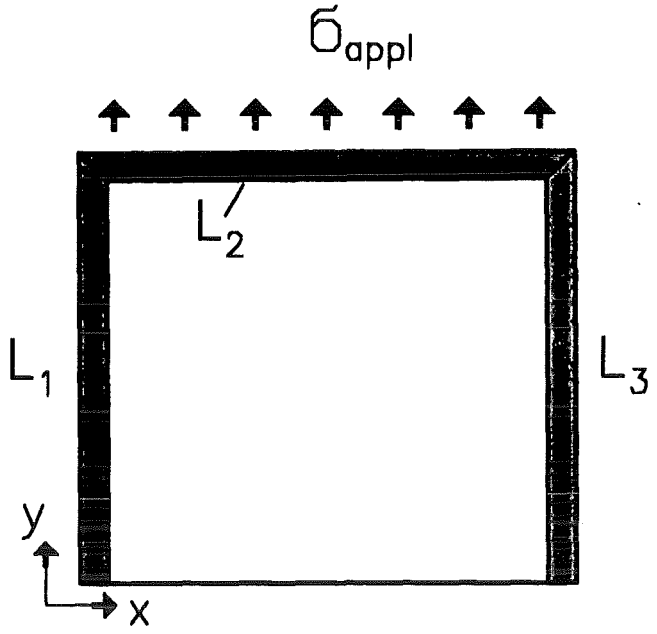

Figure 39. Boundary conditions. Boundaries for the upper part of a rectangular plate made of dissimilar materials.

5.2 Thermal loadings

The main part of this report dealed with the determination of the normalised stress intensity factor K/σ_{appl} for mechanical loading. In many cases thermal loads are responsible for the stresses in dissimilar materials. In case of the rectangular plate the stresses due to thermal mismatch are given by (see e.g. [14])

$$\sigma_{ij}^{th} = \sum_{k=1}^{\infty} K_k^{th} r^{\lambda_k - 1} g_k(\varphi) + \sigma_{0,ij} \tag{62}$$

where the superscript *th* indicates thermal loadings. The constant stress term σ_0 consists exclusively of the stress component σ_y (for y see fig.39)

$$(\sigma_{0,ij}) = \begin{pmatrix} \sigma_y & 0 \\ 0 & 0 \end{pmatrix} \tag{63}$$

It should be noted that the eigenvalues λ_k and the angular functions $g_k(\varphi)$ are independent on the special loading and, therefore, valid for mechanical and thermal loads.
It can be easily shown that the stress intensity factor relation K^{th}/σ_0 is (apart from a minus sign) identical with the corresponding relation K/σ_{appl} for mechanical loads. The boundary value problem is illustrated in fig.39 for mechanical loading. In case of mechanical loading the Airy stress function is Φ^{mech} and satisfies the boundary conditions

$$\frac{\partial^2 \Phi^{mech}}{\partial x\, \partial y} = 0 \quad \text{on} \quad L_1 \cup L_2 \cup L_3$$

$$\frac{\partial^2 \Phi^{mech}}{\partial y^2} = 0 \quad \text{on} \quad L_1 \cup L_3 \tag{64}$$

$$\frac{\partial^2 \Phi^{mech}}{\partial x^2} = \sigma_{appl} \quad \text{on} \quad L_2$$

where the first relation describes disappearing shear tractions and the second stands for disappearing σ_x tractions. The boundary conditions for thermal loading are

$$\frac{\partial^2 \Phi^{th}}{\partial x\, \partial y} = 0 \quad \text{on} \quad L_1 \cup L_2 \cup L_3$$

$$\frac{\partial^2 \Phi^{th}}{\partial y^2} = 0 \quad \text{on} \quad L_1 \cup L_3 \tag{65}$$

$$\frac{\partial^2 \Phi^{th}}{\partial x^2} = 0 \quad \text{on} \quad L_2$$

If the Airy stress function for thermal loading is expressed by the sum of two contributions

$$\Phi^{th} = \hat{\Phi}^{th} + \Phi_0 \,, \quad \Phi_0 = \frac{1}{2} x^2 \sigma_0 \tag{66}$$

the last equation of (65) can be written

$$\frac{\partial^2 \hat{\Phi}^{th}}{\partial x^2} = -\sigma_0 \quad \text{on} \quad L_2 \tag{67}$$

while the other two relations are also valid for $\hat{\Phi}^{th}$. Equation (67) can be rewritten

$$\frac{\partial^2}{\partial x^2}\left(-\frac{\sigma_{appl}}{\sigma_0}\hat{\Phi}^{th}\right) = \sigma_{appl} \quad \text{on} \quad L_2 \tag{68}$$

Comparison with the third relation of eq.(64) shows that

$$\hat{\Phi}^{th} = -\frac{\sigma_0}{\sigma_{appl}} \Phi^{mech} + f(y) \quad \text{on} \quad L_1 \cup L_2 \cup L_3 \tag{69}$$

with an arbitrary function $f(y)$. From the second relation of eq.(65) it follows

$$f(y) = C\, y \tag{70}$$

It should be noted that the function $f(y)$ does not influence the stresses. Therefore, we can set it arbitrarily as zero, i.e. $C = 0$.

$$\hat{\Phi}^{th} = -\frac{\sigma_0}{\sigma_{appl}}\,\Phi^{mech} \quad \text{on} \quad L_1 \cup L_2 \cup L_3 \tag{71}$$

The stress functions $\hat{\Phi}^{th}$ and $-\sigma_0/\sigma_{appl}\,\Phi^{mech}$ fulfill the same differential equation, eq.(1), and the same boundary conditions at all boundaries. Consequently, the uniqueness theorem ensures that the two stress functions are identical in the whole body. We obtain

$$\Phi^{th} = -\frac{\sigma_0}{\sigma_{appl}}\,\Phi^{mech} + \Phi_0 \tag{72}$$

If we express the Airy stress function in polar coordinates according to fig.1 with

$$\begin{aligned} \Phi^{mech} &= \sum_{k=0}^{\infty} K_k^{mech}\, r^{1+\lambda_k}\, g_k(\varphi) \\ \hat{\Phi}^{th} &= \sum_{k=0}^{\infty} \hat{K}_k^{th}\, r^{1+\lambda_k}\, g_k(\varphi) \end{aligned} \tag{73}$$

it follows

$$\sum_{k=1}^{\infty} \hat{K}_k^{th}\, r^{1+\lambda_k}\, g_k(\varphi) = \sum_{k=1}^{\infty} \left(-K_k^{mech}\,\frac{\sigma_0}{\sigma_{appl}} \right) r^{1+\lambda_k}\, g_k(\varphi) \tag{74}$$

Since this relation has to be valid for all (r, φ) in the body we find

$$\frac{\hat{K}_k^{th}}{\sigma_0} = -\frac{K_k^{mech}}{\sigma_{appl}} \tag{75}$$